Available online at www.sciencedirect.com
SCIENCE DIRECT®
ELSEVIER
Journal of Sound and Vibration 277 (2004) 163–203
JOURNAL OF SOUND AND VIBRATION
www.elsevier.com/locate/jsvi

Hydroelastic behaviour of a conical shell impacting on a quiescent-free surface of an incompressible liquid

Y.-M. Scolan*

Unite Hydrodynamique, Centre Mecanique Energetique, Ecole Supérieure d'Ingénieurs de Marseille, Technopôle Château Gombert, 13451 Marseille Cedex 20, France

Received 22 May 2003; accepted 26 August 2003

Abstract

Hydroelastic effects are simulated by coupling a hydrodynamic Wagner model to a linear model of elasticity for thin shells. Applications are done for a cone falling on a flat-free surface of an incompressible liquid. Both hydrodynamic and structural models are linearized on the basis of a flat disk approximation. This is justified when the deadrise angle is small. In the hydrodynamic Wagner model, the main task is to evaluate the time-varying expansion of the wetted surface. The coupling with the linear model of elasticity is achieved via a modal-based method. This means that the hydrodynamic variables must project onto the family of eigenfunctions; this is the second main difficulty of the present problem. The coupled problem is solved mainly analytically.

Special attention is paid to the energy conservation law. In particular, it is shown that kinetic energy evacuated in the jet plays as significant a role in the distribution of energy as the kinetic energy transmitted to the fluid or the kinetic and potential energies of the elastic shell.

The importance of elasticity is discussed by comparing the rigid and elastic behaviours for free drop tests. A parametric study shows the influence of each parameter: thickness, deadrise angle and drop height. Comparisons with available experimental pressure data show a reasonable agreement. On the basis of this work, lines of future research are outlined.

1. Introduction

In naval architecture and in the offshore industry, there are many situations where hydroelasticity effects due to slamming are of great interest. For example high-speed vessels, floating production storage offloading (FPSO) structures and cruisers may strongly suffer from

*Fax: 33-4-91-054615.
E-mail address: scolan@esim.imt-mrs.fr (Y.-M. Scolan).

0022-460X/$ - see front matter
doi:10.1016/j.jsv.2003.08.051

these effects. This depends on their environmental sea states (not necessarily rough) and their local stern or bow configurations.

Today, designers still cannot determine using a single model all the dimensioning loads (due to wave, current, water impact, interactions with other structures, etc.) and the resulting sea-keeping behaviour of ships or offshore structures. It is not unrealistic to think that such solvers will exist in the long term. On the one hand, sea-keeping solvers are now used for industrial purposes in a standard way. On the other hand, computational fluid dynamics solvers (for Navier–Stokes or Euler equations) are coupled through adapted algorithms to capture the free surface motion (volume of fluid, level-set, etc.). These approaches are getting more and more efficient. But to the author's knowledge they have not yet proved their ability to reproduce slamming effects with sufficient numerical stability. In particular, the pressure calculation is far from being numerically stable enough. The promising method smooth particle hydrodynamics, which is very stable in essence (see Ref. [1]), makes it possible to capture strong fluid/structure interactions. However this technique also suffers from numerical difficulties when accounting for the impermeability conditions.

Alternative approaches consist of isolating in space (locations on the hull) and time (occurrence) the slamming effects and then models can be used with a known domain of application. This paper aims to enlarge the domain of application of this approach. After identifying the initial contact point and the kinematics of a falling elastic shell, the present technique combines a structural model within the linear elasticity theory with a rather simple hydrodynamic pressure model. Among the existing hydrodynamic slamming models, the Wagner technique [2] is undoubtedly the simplest one. Basically, the continuously and rapidly expanding wet surface of the body is calculated while the body penetrates the liquid. The fluid is perfect and incompressible and the flow is irrotational. The hydrodynamic boundary value problem (BVP) is posed within the potential theory. In addition, gravity effects and surface tension effects are neglected. The reason why acoustic effects are also discarded will be discussed later. The fluid which is ejected in the jet is not modelled but the velocity and flux of the fluid in the jet can be approximated. This yields not only information on the kinetic energy which is evacuated in the jet, but also some arguments about the energy conservation law.

For two-dimensional and axisymmetric rigid bodies, linearized or generalized Wagner models are now well solved (see Refs. [3–6]). But slamming effects are three dimensional in nature and common strip theory is not reliable enough. Therefore the three-dimensional linearized Wagner problem has been developed further (see Refs. [7–9]). For arbitrary three-dimensional shapes, the problem is still open but for an elliptic paraboloid there exist exact solutions by solving the inverse Wagner problem (see Ref. [10]). When the body is elastic only simple shells can be considered. Wilkinson et al. [11] formulated the pressure distribution within a Karman technique, i.e. without accounting for the wetting correction. In Ref. [12] hydroelastic effects on the wetdeck of a catamaran are analyzed by coupling a linear elastic model (Euler or Timoshenko beam) to a linearized Wagner model through a modal decomposition of the variables (deflection and hydrodynamic pressure). Korobkin and Khabakhpasheva [13] gave more insights into this coupled hydroelastic problem. In particular they proposed a simple method of solution. On the basis of their work, the case of a cone is investigated in this paper.

The model is developed on the basis of a drastic assumption: the deadrise angle (the relative angle between the body surface and the deformed free surface) is small. This means that the BVP

can be posed onto a horizontal plane. This is known as the flat disk approximation. This assumption is crucial in order to provide (semi-)analytical solutions. If not, the only alternative approach is a numerical approach formulated for example through an integral equation for the potentials of the flow (see for example the recent work by Battistin and Iafrati [14]).

In this paper, the first section is devoted to the coupled hydroelastic problem. Special attention is paid to the energy conservation law. As for the rigid case, it is proved (see Refs. [15,16] among others) that the energy evacuated in the jet plays as significant a role in the distribution of energy as the kinetic energy transmitted to the fluid or the kinetic and potential energies of the elastic shell.

Then the obtained results are discussed. The pressure distribution acting on the cone is compared to available experimental data by Donguy [17]. Phenomena such as air cushions or entrapped air pocket are described. In conclusion, some perspectives for future research are outlined in order to improve the model and also to know better its domain of application.

2. Hydroelastic problems within the Wagner theory

The Wagner theory [2] was initially developed to calculate the pressure loads acting on floaters of seaplanes when landing. These floaters are generally elongated and therefore the corresponding two-dimensional wedge section has been studied in detail. The extension to a three-dimensional configuration is straightforward. However the problem gets more tricky. It is illustrated in Fig. 1. In the upper part the actual shape is shown as it penetrates, at time t, an initially flat free surface of liquid. The locally deformed free surface is drawn. The jet is not reproduced. For the sake of

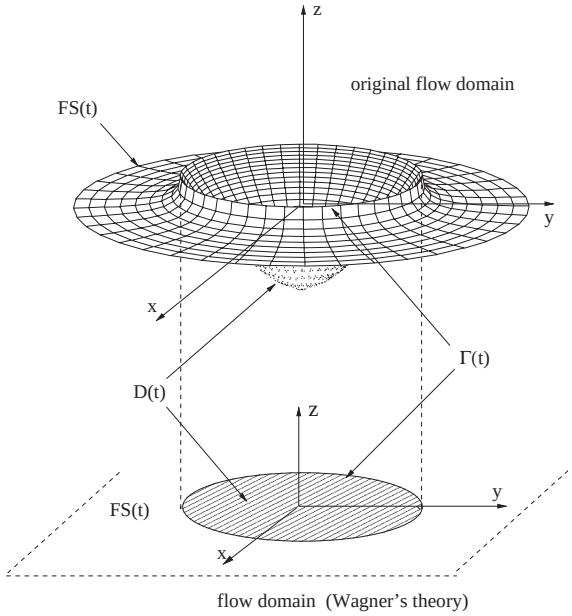

Fig. 1. Hydrodynamic Wagner problem: original flow domain and linearized domain following the assumption of small deadrise angle. The body falls vertically (z direction). The computational domain is bounded with the horizontal plane. This plane is decomposed into $FS(t)$; the free surface, and $D(t)$; the wet surface of the body. These two surfaces are separated with $\Gamma(t)$: the contact line. The jet is not reproduced in the figure.

visibility, the scale is stretched in the vertical direction. The picture illustrates how the problem is linearized. The linearization of the boundary conditions implies that the surfaces are projected onto a horizontal plane which becomes the upper boundary of the computational fluid domain. Two parts are identified: the free surface $FS(t)$, which extends to infinity and the wet body surface $D(t)$. Both $FS(t)$, and $D(t)$ depend on time t. They are separated by the so-called contact line $\Gamma(t)$. The time evolution of $\Gamma(t)$ is such that the closed curves $\Gamma(t_1)$ and $\Gamma(t_2)$ have no intersection points as long as $t_1 \neq t_2$. The velocity of the expanding surface $D(t)$ is the most important parameter in the present problem. For a symmetric two-dimensional section or an axisymmetric body (cone, sphere, etc.), one has to calculate only a scalar quantity; this is called the wetting correction.

The linearization is based on the assumption that the deadrise angle is small. The value 4° is commonly accepted as the lower limit. Below this value, ventilation effects may occur leading to a non-homogeneous fluid. Above 20°, comparisons with experimental data show that this model fails. Zhao and Faltinsen [4] hence formulated the problem by imposing the boundary condition on the exact wet surface. However, in that case, the method of solution is fully numerical unless simple shapes are considered through geometric transformations (see Refs. [18–20], among others). Here attention is focused on the methods of solution usable at preliminary design stages. Hence analytical methods are preferred since they usually require small computer resources.

When the body is elastic, a model of elasticity must be introduced. The decoupled problem consists in solving separately the hydrodynamic problem with a rigid body on the one hand and a structural problem on the other. This approach provides results but it is known that information is lost (see Ref. [21]). It is preferred here to solve the fully coupled hydroelastic problems: the Wagner problem on the one hand and a linear model of elasticity on the other.

The coupling of the hydrodynamic and elastic problems is not straightforward. This is due to the nature of the hydrodynamic excitation, i.e. the pressure. As a matter of fact, the pressure does not act on the whole surface of the shell but just acts on its wet part. Within the Wagner approach, it is known that the distribution of pressure has a strong peak close to the contact line and furthermore this line evolves very rapidly in time.

These problems are described in the following developments. The elastic model is first detailed on the basis of a modal decomposition. The hydrodynamic problem is then solved providing a way to determine the velocity at which the wet surface expands. The coupling of the two models follows from the decomposition of the velocity potential and/or displacement potential on a family of eigenfunctions. Finally special attention is paid to the energy conservation law.

2.1. Elastic model

Among the existing elastic models, the linear model of the Euler type is the simplest one to implement. For the present thin conical shell the surface of the cone is linearized. The linearization follows from the assumption that the deadrise angle β is small. This approximation is consistent with the hydrodynamic problem. However it can be criticized from the structural point of view. More sophisticated models can be used which can handle more accurately the actual shape of the cone. At least the curvature of shallow spherical shells can be accounted for by using Marguerre's formulation [22]. For such shells with clamped edge conditions, applications can be found in Soliman and Gonçalves [23]. In their approach the governing partial differential equations are formulated for the vertical displacement and the stress function. In Wan's theory [24] the

formulation for conical shells is also available. The coupling of these equations to the present hydrodynamic Wagner model could be considered in future works.

Here within the retained assumptions, the deflection is calculated with respect to the horizontal plane as sketched in Fig. 2 where the physical and linearized domains are drawn. The deflection $w(x, y, t)$ is expressed in terms of known eigenfunctions. For a cone falling along its axis of symmetry, the eigenmodes are those of a flat circular shell. Calling $w_m(x, y)$ the eigenfunctions, the deflection can be calculated from a breakdown where space and time variations are separated:

$$w(x, y, t) = \sum_{n}^{\infty} A_n(t) w_n(x, y). \tag{1}$$

$A_n(t)$ denotes the amplitudes of each mode shape and they only depend on time t. In the following the variable $\mathbf{A}$ will denote the vector with components $A_n(t)$. Only axisymmetric modes are retained, hence the eigenmodes $w_n(x, y)$ reduce to a function of the radial co-ordinate $r = \sqrt{x^2 + y^2}$. These functions also depend on the boundary conditions. It is reasonable to impose a fixed centre with an actual clamping condition in order to reproduce the strong rigidity of the cone at its centre. Along its outer boundary $r = R$, a clamping condition is also imposed. There are two reasons for that: (1) the shell can respond with its axisymmetric modes only, and (2) experimental data (see Ref. [17]) exist for a configuration close to the present one. The boundary conditions are summed up as follows:

$$\begin{cases} w(r, t) = w_{,r}(r, t) = 0 & \text{at centre } r = 0, \\ w(r, t) = w_{,r}(r, t) = 0 & \text{outer boundary } r = R. \end{cases} \tag{2}$$

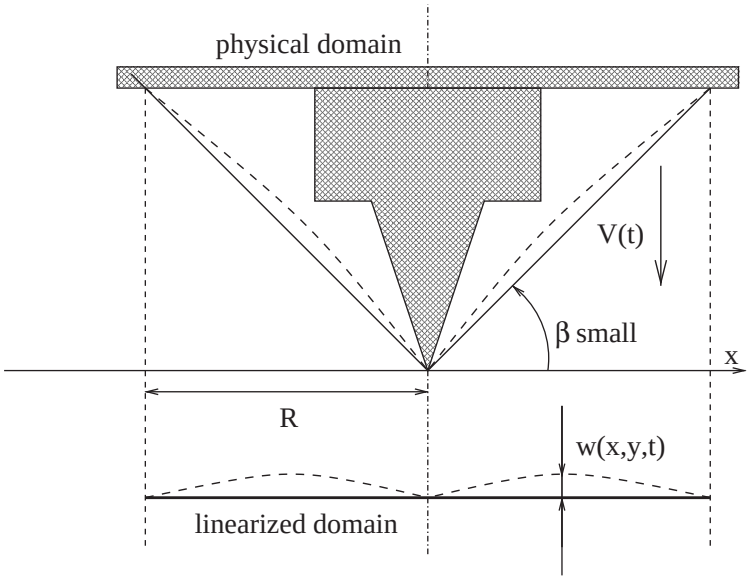

Fig. 2. Physical domain and linearized computational domain following the assumption of small deadrise angle β. The shell and its supporting body fall vertically with velocity $V(t)$. The deflection $w(x, y, t)$ depends on time t and it is measured in the horizontal plane from the undeformed shell at the point (x, y). The cone is clamped at the tip and along its outer edge. For axisymmetric cone the edge is defined by $R = \sqrt{x^2 + y^2}$.

The eigenmodes are calculated after solving the homogeneous partial differential equation for $W(r,t)$:

$$D\boldsymbol{\Delta\Delta}W + \rho_d H\ddot{W} = 0, \quad D = \frac{EH^3}{12(1-\nu^2)}, \tag{3}$$

where ρ_d is the density of the shell and H is its thickness. Young's modulus is E and the Poisson coefficient is denoted by ν. Space derivatives appear in the double Laplacian operator $\boldsymbol{\Delta\Delta}$ and double dots denote the second time derivative. Solutions are sought as harmonic functions in time:

$$W(r,t) = W(r)\sin\omega t, \tag{4}$$

leading to the space differential equation for $W(r)$;

$$D\boldsymbol{\Delta\Delta}W - \omega^2\rho_d HW = 0, \tag{5}$$

where the circular frequency ω is then introduced with the associated number k so that

$$(k/R)^4 = \frac{\rho_d H\omega^2}{D}. \tag{6}$$

It is known that the elementary solutions of Eq. (5) are expressed as a linear combination of the zeroth order Bessel and modified Bessel functions since only axisymmetric modes can respond:

$$W(r) = A\mathrm{J}_0\left(\frac{kr}{R}\right) + B\mathrm{I}_0\left(\frac{kr}{R}\right) + C\mathrm{Y}_0\left(\frac{kr}{R}\right) + D\mathrm{K}_0\left(\frac{kr}{R}\right), \tag{7}$$

where one of the constants (A,B,C,D) can be arbitrarily chosen. A singularity at the centre $r=0$ occurs in the boundary conditions (2). It is removed by imposing $D = \frac{2}{\pi}C$ in Eq. (7). The clamping condition at $r=0$ yields $A+B=0$ and the remaining conditions on the edge provide the condition

$$J(k) = \frac{(\mathrm{J}_0(k) - \mathrm{I}_0(k))}{(\mathrm{J}_1(k) + \mathrm{I}_1(k))} - \frac{\left(\mathrm{Y}_0(k) + \frac{2}{\pi}\mathrm{K}_0(k)\right)}{\left(\mathrm{Y}_1(k) + \frac{2}{\pi}\mathrm{K}_1(k)\right)} = 0, \tag{8}$$

whose zeroes define an infinite set of non-dimensional numbers $(k_m)_{m\geqslant 1}$. The shape function $W(r)$ must hence be numbered and the resulting family of eigenfunctions reduces to

$$w_m(r) = C_m\left[\mathrm{J}_0\left(\frac{k_m r}{R}\right) - \mathrm{I}_0\left(\frac{k_m r}{R}\right)\right] - \left[\mathrm{Y}_0\left(\frac{k_m r}{R}\right) + \frac{2}{\pi}\mathrm{K}_0\left(\frac{k_m r}{R}\right)\right], \tag{9}$$

with the coefficients

$$C_m = \frac{\left(\mathrm{Y}_0(k_m) + \frac{2}{\pi}\mathrm{K}_0(k_m)\right)}{(\mathrm{J}_0(k_m) - \mathrm{I}_0(k_m))} = \frac{\left(\mathrm{Y}_1(k_m) + \frac{2}{\pi}\mathrm{K}_1(k_m)\right)}{(\mathrm{J}_1(k_m) + \mathrm{I}_1(k_m))}. \tag{10}$$

It should be noted that the second derivative of $w_m(r)$ is singular at the origin. Consequently the strains and stresses are also asymptotically singular at the origin. By using the boundary conditions (2), it can be shown that the singularity behaves as $\log r$. The present idealized configuration must be considered as a limiting case of the more physical configuration where the elastic disk is clamped along a small disk of finite radius, denoted ε and such that $\varepsilon/R \to 0$ asymptotically. For finite radius ε all quantities are also finite. It can be checked that the eigennumbers k (which follow from Eq. (8) and which are calculated below) are the limit of $k(\varepsilon)$ when $\varepsilon/R \to 0$. This is discussed in Ref. [25] or in Ref. [26]. It is concluded that the strains and stresses can be very high in the vicinity of the tip but they are concentrated at a single point of zero radius. The resulting global stress is however finite at the tip since it behaves as $\varepsilon\log\varepsilon$ asymptotically.

It should be noted that the eigennumbers k_n can be approximated for large n; however, the numerical computation provides them with a quite sufficient degree of accuracy. The solutions $(w_n)_{n=1,\infty}$ compose a complete set of orthogonal functions for the inner product

$$\int_0^R w_n(r)w_m(r)r\,\mathrm{d}r = \delta_{nm}U_m = \begin{cases} U_m & \text{if } m = n, \\ 0 & \text{if } m \neq n. \end{cases} \tag{11}$$

2.2. Hydrodynamic Wagner model

The present application is a simplified case of the theory exposed in Korobkin and Scolan [27]. Numerical calculations appear in Appendix A.

The boundary value problem (BVP) is solved in time for $t \geqslant 0$ where the origin $t = 0$ corresponds to the instant at which the body starts its penetration into the liquid. The body has either a constant velocity of penetration or it may fall freely in vacuum over an initial height h_c. This yields the velocity at the initial contact instant to be $V_{ini} = \sqrt{2gh_c}$. Within potential flow theory, the BVP is formulated in terms of the displacement potential ϕ; this is the time integral of the velocity potential $\varphi = \phi_{,t}$. It is calculated in the whole fluid domain $\Omega(t)$ limited on its upper side with the free surface $FS(t)$ and the wet part of the body $D(t)$. This BVP is mixed. The Bernoulli equation expressed on $FS(t)$ reduces it to a homogeneous Dirichlet condition for φ and ϕ, by neglecting both the gravity and the quadratic term $(\nabla\varphi)^2$. This means that all streamlines arrive at the free surface at a right angle; this is due to the linearization of the free surface on its position at rest. As a consequence the fluid at the free surface may have only a vertical motion and the flow can be extended in the upper half plane by symmetry; this is the so-called "flat disk approximation". On $D(t)$ a Neumann condition results from the impermeability of the body. Fig. 3 shows the physical and linearized domains and the corresponding notations. The resulting BVP now reads

$$\begin{cases} \Delta\phi = 0 & \tilde{z} < 0, \\ \phi = 0 & \text{on } \rho > 1 \text{ and } \tilde{z} = 0, \\ \phi_{,\tilde{z}} = a(t)[-h(t) + f(a(t)\rho) + w(a(t)\rho, t)] & \text{on } \rho < 1 \text{ and } \tilde{z} = 0, \\ \phi \to 0 & (\rho^2 + \tilde{z}^2) \to \infty, \end{cases} \tag{12}$$

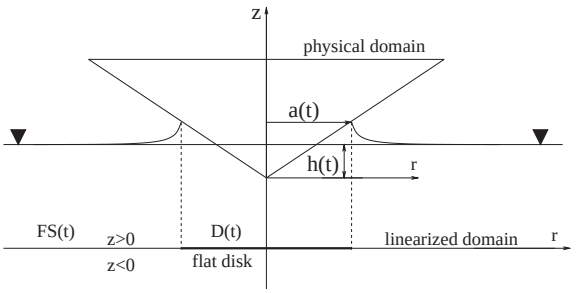

Fig. 3. Flat disk approximation within Wagner theory.

where the vertical and radial co-ordinates are made non-dimensional with $a(t)$; $\tilde{z} = z/a(t)$, $\rho = r/a(t)$. At time t the body penetrates the liquid with a draft $h(t)$. The equation $z = f(r)$ defines a generatrix of the cone measured from the apex, such that $f(r) = r\tan\beta$. The usual way to solve this problem is to perform a Hankel transformation of the variable (see Ref. [28]). The displacement potential is sought in the form

$$\phi(\rho, \tilde{z}, t) = \int_0^\infty G(\lambda, t) \mathrm{e}^{\lambda\tilde{z}} \mathrm{J}_0(\lambda\rho)\,\mathrm{d}\lambda, \tag{13}$$

and must verify the two boundary conditions. This gives

$$\int_0^\infty G(\lambda, t)\mathrm{J}_0(\lambda\rho)\,\mathrm{d}\lambda = 0 \quad \text{for } \rho > 1, \tag{14}$$

and

$$\int_0^\infty \lambda G(\lambda, t)\mathrm{J}_0(\lambda\rho)\,\mathrm{d}\lambda = a(t)(-h(t) + f(a(t)\rho) + w(a(t)\rho, t)) \tag{15}$$

$$= \kappa(a(t)\rho, t) \quad \text{for } \rho < 1. \tag{16}$$

After some algebra the function $G(\lambda, t)$ appears as a particular case of Titchmarsh's solutions (see Ref. [29, p. 86]):

$$G(\lambda, t) = \sqrt{\frac{2\lambda}{\pi}} \int_0^1 u^{\frac{3}{2}} \mathrm{J}_{1/2}(u\lambda)\,\mathrm{d}u \int_0^{\frac{\pi}{2}} \sin\alpha\,\kappa(a(t)u\sin\alpha, t)\,\mathrm{d}\alpha, \tag{17}$$

where κ (see Eq. (16)) denotes the right side of the Neumann condition on the wetted surface $\rho < 1$. The function $G(\lambda, t)$ is then introduced in Eq. (13) and the integration in λ is performed by using equation AS[1] 11.4.41 to give

$$\phi(\rho, 0, t) = \int_1^{1/\rho} \frac{\chi(\rho v, t)\,\mathrm{d}v}{\sqrt{v^2 - 1}}, \quad (0 < \rho < 1), \tag{18}$$

with

$$\chi(\mu, t) = \frac{2}{\pi} \int_0^\mu \frac{\sigma\kappa(a(t)\sigma, t)\,\mathrm{d}\sigma}{\sqrt{\mu^2 - \sigma^2}}. \tag{19}$$

The function $\chi(\mu, t)$ can be further developed for the cone as

$$\chi(\mu, t) = \frac{2a}{\pi}\left[-h\mu + \frac{\pi}{4} a\mu^2 \tan\beta + \mu \sum_{n=1}^{\infty} A_n(t) \int_0^1 \frac{x w_n(a\mu x)\,\mathrm{d}x}{\sqrt{1 - x^2}}\right]. \tag{20}$$

[1] The acronym AS refers to formulæ in Abramowitz and Stegun [30].

The displacement potential then reads[2];

$$\phi(\rho,0,t) = -\frac{2ah}{\pi}\sqrt{1-\rho^2} + \frac{a^2\tan\beta}{4}\left[\rho^2\,\mathrm{Argch}\frac{1}{\rho} + \sqrt{1-\rho^2}\right] + \frac{2a\rho}{\pi}\sum_{n=1}^{\infty} A_n(t)\int_1^{1/\rho}\frac{v\,\mathrm{d}v}{\sqrt{v^2-1}}\int_0^1 \frac{x w_n(axv\rho)\,\mathrm{d}x}{\sqrt{1-x^2}}. \tag{21}$$

The radial gradient of ϕ represents the radial displacement of the fluid. It is singular at $\rho = 1$ but it must be continuous along the intersection line. This condition is satisfied if and only if $\phi_{,\rho}(1,0,t) = 0$. The so-called Wagner condition thus reads

$$\int_0^{\frac{\pi}{2}} \sin\alpha\kappa(a(t)\sin\alpha, t)\,\mathrm{d}\alpha = 0, \tag{22}$$

which is used to calculate $a(t)$. For the cone, the Wagner condition is turned into

$$\mathbf{AQ} = h(t) - a\frac{\pi}{4}\tan\beta, \tag{23}$$

where the vector $\mathbf{Q}$ has components

$$Q_n(a) = \int_0^1 \frac{x w_n(ax)\,\mathrm{d}x}{\sqrt{1-x^2}} = \int_0^{\pi/2} \sin\theta w_n(a(t)\sin\theta)\,\mathrm{d}\theta. \tag{24}$$

The numerical calculation of the coefficients $Q_n(a)$ is detailed in Section A.1. The displacement potential can be further developed but it is not used any longer. From expression (21) one calculates the velocity potential by using $\varphi = \phi_{,t}$;

$$\varphi(r,a) = -\frac{2V(t)}{\pi}\sqrt{a^2-r^2} + \dot{\mathbf{A}}\mathbf{\Phi} = \varphi_0(r,a,t) + \varphi_e(r,a,t), \tag{25}$$

where the first component (φ_0) corresponds to the velocity potential of the rigid disk with radius $a(t)$. The second term (φ_e) is the modal decomposition of the potentials with components (see Section A.4)

$$\Phi_n(r,a) = \frac{2r}{\pi}\int_1^{a/r}\frac{v\,\mathrm{d}v}{\sqrt{v^2-1}}\int_0^1 \frac{x w_n(rxv)\,\mathrm{d}x}{\sqrt{1-x^2}}. \tag{26}$$

The free surface elevation is obtained from the vertical gradient of the displacement potential calculated on the free surface $z = 0$;

$$\eta(r,t) = \phi_{,z}(r,z,t)|_{z=0} = \frac{1}{a}\int_0^{\infty} \lambda G(\lambda,t)\mathrm{J}_0(\lambda\rho)\,\mathrm{d}\lambda, \tag{27}$$

[2] It is worth noting that Argch $1/\rho$ can be also written as $\log\left(1+\sqrt{1-\rho^2}\right) - \log\rho$.

where G is obtained from Eq. (17). The λ-integration is performed by using equation GR[3] 6.575.1 to give

$$\eta(r,t) = -\frac{1}{a}\int_0^1 \frac{v\chi(v,t)\,\mathrm{d}v}{(\rho^2-v^2)^{3/2}}, \quad (\rho > 1), \tag{28}$$

where χ of Eq. (20) is introduced in the integrand of Eq. (28), this yields the following result:

$$\eta(r,t) = \frac{2h(t)}{\pi}\,\mathrm{Y}_2(\rho) - \frac{a\tan\beta}{2}\,\mathrm{Y}_3(\rho) - \frac{2}{\pi}\mathbf{AE}, \tag{29}$$

with the tabulated formalæ

$$\mathrm{Y}_n(\rho) = \int_0^1 \frac{v^n\,\mathrm{d}v}{(\rho^2-v^2)^{3/2}}, \quad E_n(\rho,a) = \int_0^{\arcsin(1/\rho)} \tan^2\alpha\, Q_n(a\rho\sin\alpha)\,\mathrm{d}\alpha. \tag{30}$$

Since the partial differential equation (3) is of second order in time, one should note that the pressure is not explicitly required in the coupled problem but its time integral, that is to say the velocity potential. As a consequence the modal formulation of the pressure is avoided. The pressure distribution is hence calculated a posteriori and follows from Bernoulli's equation;

$$p = -\rho_f \varphi_{,t} = -\rho_f(\dot{\varphi}_0(r,a,t) + \ddot{\mathbf{A}}\mathbf{\Phi} + \dot{\mathbf{A}}\dot{\mathbf{\Phi}}), \tag{31}$$

where ρ_f is the density of the fluid. This expression is singular at $r = a(t)$ i.e. at the spray root. The singular part of the pressure is isolated having in view the coupling with the local solution of Wagner [2].

$$P_{sing} = \frac{2}{\pi}\rho_f a\dot{a}\frac{V - \dot{\mathbf{A}}\mathbf{Q}}{\sqrt{a^2-r^2}}. \tag{32}$$

Fig. 4 illustrates the fluid motion in the vicinity of the contact line $r = a(t)$. The local solution calculated by Wagner [2] in the spray root is two dimensional but it is proved (see Refs. [32,33]) that it can be matched to the present axisymmetric solution. The flow is described in a co-ordinate system (O,ξ,η) attached to the spray root as sketched in Fig. 5. The asymptotic expressions of the velocity potential and the pressure when $\xi \to 0$ are written as follows:

$$\varphi_{root} \approx -4U\sqrt{\frac{\delta|\xi|}{\pi}}, \quad p_{root} \approx 2\rho_f U^2\sqrt{\frac{\delta}{\pi|\xi|}}. \tag{33}$$

They are matched to the solution (32) given above, hence yielding U, the velocity of the fluid in the jet and δ the thickness of the jet;

$$U = \dot{a}, \quad \delta = \frac{a}{2\pi\dot{a}^2}(V - \mathbf{Q}(a)\dot{\mathbf{A}})^2. \tag{34}$$

The obtained distribution of pressure predicts a maximum at the stagnation point (at the origin of the co-ordinate system attached to the spray root)

$$P_{max} = \frac{1}{2}\rho_f\dot{a}^2, \tag{35}$$

[3] The acronym GR refers to formulæ in Gradshteyn and Ryzhik [31].

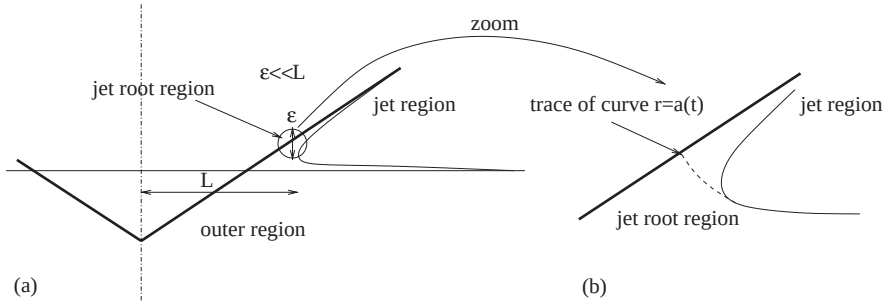

Fig. 4. (a) Fluid motion in the vicinity of the contact line $r = a(t)$. The jet root region has a length scale ε small compared to the length scale of the wet body $L \approx a(t)$. (b) Zoom on the spray root region where the curve $r = a(t)$ is defined as the contact line separating the free surface and the body wet surface.

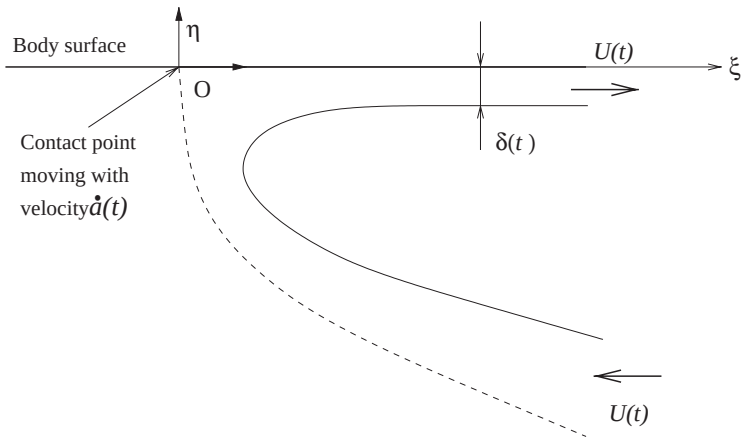

Fig. 5. Description of the spray root solution within a co-ordinate system (O, ξ, η) attached to the contact line $r = a(t)$. The spray root is characterized with U the velocity of the fluid in the jet and δ the thickness of the jet.

consistently with the rigid case. A uniformly valid distribution of pressure is obtained up to $r = a^+$ (i.e. within the spray root) from the composite formulation by Zhao and Faltinsen [4]

$$p(r,t) = -\rho_f \dot{\varphi}_0 - \rho_f \sum_{n=1}^{\infty} \frac{\mathrm{d}}{\mathrm{d}t} \dot{\mathbf{A}}\mathbf{\Phi} + P_{root} - \frac{1}{\pi}\rho_f \dot{a}(V - \mathbf{Q}\dot{\mathbf{A}})\sqrt{\frac{2a}{a-r}}, \tag{36}$$

where the last term cancels the singularity at $r = a$. This is the asymptotic expression of P_{sing} (see Eq. (32)) along the contact line, i.e., when $r \to a$. This formulation yields a uniformly valid distribution of pressure, in particular it catches the maximum of pressure through the component P_{root} which reads

$$P_{root} = 2\rho\dot{a}^2 \frac{|\tau|^{1/2}}{(1+|\tau|^{1/2})^2}, \quad \text{with } r - a = \frac{\delta}{\pi}(-\log|\tau| - 4|\tau|^{1/2} - |\tau| + 5), \quad r > a. \tag{37}$$

Consistently with Newman [34, pp. 132–134], the force follows from the integral

$$\vec{\mathbf{F}} = -\rho_f \frac{\mathrm{d}}{\mathrm{d}t} \int_{D(t)} \varphi \vec{\mathbf{n}} \, \mathrm{d}s, \tag{38}$$

where the normal $\vec{\mathbf{n}}$ is taken to be positive when pointing out from the fluid volume, thus yielding $F(t) = \vec{\mathbf{F}} \cdot \vec{\mathbf{z}}$. Due to the boundary condition on the free surface, integral operator and time derivative permute to give

$$F(t) = 2\pi \int_0^{a(t)} p(r,t) r \, \mathrm{d}r. \tag{39}$$

As a first approximation, Eq. (31) provides the pressure to integrate. After some algebra this yields

$$F(t) = \rho_f \frac{\mathrm{d}}{\mathrm{d}t}\left(\frac{4}{3} a^3 V\right) - \frac{\mathrm{d}}{\mathrm{d}t}(\dot{\mathbf{A}}\mathbf{R}(a)), \tag{40}$$

with the vector $\mathbf{R}(a)$ defined by its coefficients (see Section A.5)

$$R_n(a) = 2\pi\rho_f \int_0^a \Phi_n(r,a) r \, \mathrm{d}r = 4\rho_f \int_0^a x^2 Q_n(x) \, \mathrm{d}x. \tag{41}$$

Its time derivative of $R_n(a)$ is directly provided by the formula

$$\dot{R}_n(a) = 4\rho_f \dot{a} a^2 Q_m(a). \tag{42}$$

It is worth noting that $F(t)$ appears as the time derivative of two terms. One can recognize two components. The first component (denoted F_r) is the usual impact force for the rigid case

$$F_r(t) = \frac{\mathrm{d}}{\mathrm{d}t}(M_a V), \quad \text{with } M_a = \frac{4}{3}\rho_f a^3, \tag{43}$$

where M_a is the added mass of the circular disk with radius $a(t)$. The second component takes into account the elasticity and can be turned into

$$F_e(t) = -\ddot{\mathbf{A}}\mathbf{R}(a) - \dot{M}_a \mathbf{Q}\dot{\mathbf{A}}. \tag{44}$$

2.3. Solution of the coupled hydroelastic problem

The partial differential equation which governs the deflection $w(r,t)$ is

$$D\boldsymbol{\Delta}\boldsymbol{\Delta} w + \rho_d H(\ddot{w} - \dot{V}) = p(r,t), \tag{45}$$

where the acceleration $\dot{V}$ can only vary in time and it corresponds to the acceleration of the body on which the shell is clamped. As $\dot{V}$ is also unknown, one needs an additional equation which is the Newton law

$$M_c \dot{V} = [M_c \gamma] - F(t), \tag{46}$$

where the brackets mean that the acceleration due to gravity γ is usually neglected. By using Eq. (40), Newton's law can be time integrated thus yielding an explicit expression for the velocity

$$V(t) = V^{\bigstar}(t) + \frac{\dot{\mathbf{A}}\mathbf{R}(a)}{(M_c + M_a)}, \quad \text{with } V^{\bigstar}(t) = \frac{M_c(\gamma t + V_{ini})}{(M_c + M_a)}. \tag{47}$$

The differential system now combines Eqs. (23), (45) and (47) for the unknowns $(a(t), V(t), \mathbf{A})$. Following Korobkin and Khabakhpasheva [13] a new variable is introduced:

$$Dq(r,t) = -\rho_d H(\dot{w} - V + V_{ini}) - \rho_f \varphi, \quad \dot{q} = \mathbf{\Delta\Delta} w. \tag{48}$$

It is first expressed in terms of the eigenfunctions $w_n(r)$;

$$q(r,t) = \sum_n^{\infty} q_n(t)(k_n/R)^4 w_n(r), \tag{49}$$

then introduced into Eq. (45). The resulting equation is projected on each vector w_m of the family by using the inner product (11)

$$\mathbf{Zq} + \mathbf{g}(a) = (\boldsymbol{\lambda} - \mathbf{W}(a))\dot{\mathbf{A}} - \mathbf{O}(V - V_{ini}), \quad \dot{\mathbf{q}} = \mathbf{A}, \tag{50}$$

where the matrices $\boldsymbol{\lambda}$, $\mathbf{W}(a)$, $\mathbf{Z}$ and vectors $\mathbf{g}(a)$, $\mathbf{O}$ have coefficients

$$W_{mn}(a) = \frac{2a^3}{\pi}\int_0^1 z^2 Q_m(az)Q_n(az)\,\mathrm{d}z, \quad g_m(a) = \int_0^{a(t)} \varphi_0(r,a,t)w_m(r)r\,\mathrm{d}r, \tag{51}$$

$$\lambda_{mm} = -H\frac{\rho_d}{\rho_f}U_m, \quad Z_{mm} = \frac{D}{\rho_f}\left(\frac{k_m}{R}\right)^4 U_m, \quad O_m = -\frac{\rho_d H}{\rho_f}\int_0^R r w_m(r)\,\mathrm{d}r = -\frac{\rho_d H}{\rho_f}O_m^{\bigstar}. \tag{52}$$

The calculations of $g_m(a)$ and $W_{mn}(a)$ are detailed in Appendix A and their variations are shown as well. The final time differential system now reads

$$\begin{cases} \dot{\mathbf{A}} = [\boldsymbol{\lambda} - \mathbf{W}(a) + \mathbf{S}(a)]^{-1}[\mathbf{Zq} + \mathbf{g}(a) + \mathbf{O}(V^{\bigstar} - V_{ini})] = F(a,q), \\ \dot{\mathbf{q}} = \mathbf{A}, \end{cases} \tag{53}$$

where $\mathbf{S}(a)$ denotes a matrix which is the dyadic product of vectors $\mathbf{O}$ and $\mathbf{R}$;

$$S_{mn} = \frac{O_m R_n(a)}{(M_c + M_a)}. \tag{54}$$

As stated earlier, $a(t)$ is a monotonic function of time t with an additional constraint that $\mathrm{d}a/\mathrm{d}t > 0$. The limiting case $\mathrm{d}a/\mathrm{d}t = 0$ means that the elastic falling shell undergoes large deflections, which is far beyond the initial assumptions. Another limiting case may occur when $\mathrm{d}t/\mathrm{d}a = 0$ and this case will be discussed later in Section 3.2. Between these two non-physical limits, when $a(t)$ varies "normally", it is advantageous to change the variable a instead of t and the Wagner condition provides the Jacobian of the transformation

$$\frac{\mathrm{d}t}{\mathrm{d}a} = \frac{\pi\tan\beta/4 + \mathbf{Q}'(a)\mathbf{A}}{V(t) - \mathbf{Q}(a)\dot{\mathbf{A}}}. \tag{55}$$

Then the differential system (53) is turned into

$$\begin{cases} \dfrac{\mathrm{d}\mathbf{A}}{\mathrm{d}a} = \dfrac{\mathrm{d}t}{\mathrm{d}a}\mathbf{F}(a,q), \\ \dfrac{\mathrm{d}\mathbf{q}}{\mathrm{d}a} = \dfrac{\mathrm{d}t}{\mathrm{d}a}\mathbf{A}. \end{cases} \tag{56}$$

A standard explicit Euler scheme is stable enough for the present numerical integration.

2.4. Energy conservation law

For the rigid case the following identity relates the time rate of the different energy components:

$$\frac{\mathrm{d}}{\mathrm{d}t}[K(t) - E_{kf}(t)] = \frac{1}{2} V^2(t) \frac{\mathrm{d}M_a}{\mathrm{d}t}. \tag{57}$$

$E_{kf}(t)$ is the kinetic energy of the liquid flow in the outer region of the jet, $E_{kf}(t) = \frac{1}{2} M_a(t) V^2(t)$ and $K(t)$ is the work done to oppose the hydrodynamic force on the entering blunt body. As explained in Ref. [32], during the initial stage of the water impact, the added mass of the expanding flat disk $D(t)$ increases, $\mathrm{d}M_a/\mathrm{d}t > 0$. Therefore, $E_{kf}(t) < K(t)$, which is usually considered as an indication that part of the energy is "lost" during the impact. It has been proved that the flux of energy in the right-hand side of Eq. (57) is equal to the flux of kinetic energy through the jet E_{jet} for some particular three-dimensional shapes as an elliptic paraboloid. Those shapes are more general than an axisymmetric cone and their results can hence be used. However new difficulties appear due to the elasticity of the body. But one hopes that taking into account the energy evacuated in the jet, the energy conservation law is also satisfied. Along these lines, one must identify additional components: the potential and kinetic energies of the elastic body, E_{ps} and E_{ks}, respectively. In order to avoid the time integration, the conservation law will be checked for the time rate of the energy components.

The simplest quantity is $\dot{E}_{jet}$ since it follows from the characteristics of the jet, that is to say its thickness δ and the velocity of the fluid in the jet $\dot{a}$ given by Eqs. (34). By using the previous notations the time rate of E_{jet} is

$$\dot{E}_{jet} = 2\rho_f \dot{a} a^2 (V - \mathbf{Q}\dot{\mathbf{A}})^2 = \frac{1}{2} \dot{M}_a V^2 - V\dot{\mathbf{R}}\dot{\mathbf{A}} + \pi\rho_f \dot{\mathbf{A}}\dot{\mathbf{W}}\dot{\mathbf{A}}. \tag{58}$$

The fluid kinetic energy follows from the integration of the square velocity throughout the fluid domain ($z<0$)

$$\dot{E}_{kf} = \frac{1}{2}\rho_f \frac{\mathrm{d}}{\mathrm{d}t}\left[\int_{(z<0)} (\vec{\boldsymbol{\nabla}}\varphi)^2 \,\mathrm{d}v\right]. \tag{59}$$

Invoking Green's first identity and by using the boundary conditions on the contour of the fluid domain, $\dot{E}_{kf}$ can be turned into

$$\dot{E}_{kf} = \frac{1}{2}\rho_f \frac{\mathrm{d}}{\mathrm{d}t}\left[\int_{D(t)} \varphi\varphi_{,z} \,\mathrm{d}s\right], \tag{60}$$

where the velocity potential φ is formulated according to Eq. (25). Their corresponding vertical gradients on the wet body surface $D(t)$ are also known:

$$\varphi_{0,z} = -V(t), \quad \varphi_{e,z} = \dot{w}(r,t), \quad \text{on } z = 0. \tag{61}$$

As the potentials $\varphi_0(r,z,t)$ and $\varphi_e(r,z,t)$ are harmonic in the fluid domain ($z<0$), and by using their associated boundary condition on the free surface, the second Green's identity shows that

$$\int_{D(t)} \varphi_e \varphi_{0,z} \,\mathrm{d}s = \int_{D(t)} \varphi_0 \varphi_{e,z} \,\mathrm{d}s, \tag{62}$$

hence one obtains

$$\dot{E}_{kf} = \frac{\mathrm{d}}{\mathrm{d}t}\left[\frac{1}{2} M_a V^2 - V\dot{\mathbf{A}}\mathbf{R} + \pi\rho_f \dot{\mathbf{A}}\mathbf{W}\dot{\mathbf{A}}\right], \tag{63}$$

which is turned into

$$\dot{E}_{kf} = \frac{1}{2}\dot{M}_a V^2 + M_a V\dot{V} - \dot{V}\dot{\mathbf{A}}\mathbf{R} - V\ddot{\mathbf{A}}\mathbf{R} - V\dot{\mathbf{A}}\dot{\mathbf{R}} + 2\pi\rho_f \ddot{\mathbf{A}}\mathbf{W}\dot{\mathbf{A}} + \pi\rho_f \dot{\mathbf{A}}\dot{\mathbf{W}}\dot{\mathbf{A}}. \tag{64}$$

On the other hand the projection of the partial differential equation (50) which governs the plate deflection is rearranged. This equation is time differentiated and both sides are multiplied by $2\pi\dot{A}_m$. Then a summation is performed throughout the indices m:

$$2\pi D \sum_m^\infty \left(\frac{k_m}{R}\right)^4 U_m A_m \dot{A}_m + 2\pi H\rho_d \sum_m^\infty U_m \dot{A}_m \ddot{A}_m - 2\pi H\rho_d \dot{V} \sum_m^\infty O_m^\star \dot{A}_m$$

$$= -2\pi\rho_f(\dot{\mathbf{A}}\dot{\mathbf{W}}\dot{\mathbf{A}} + \dot{\mathbf{g}}\dot{\mathbf{A}} + \dot{\mathbf{A}}\mathbf{W}\ddot{\mathbf{A}}). \tag{65}$$

One can recognize on the left side the potential and kinetic energies of the elastic body, namely

$$\dot{E}_{ps} = 2\pi D \sum_m^\infty \left(\frac{k_m}{R}\right)^4 U_m A_m \dot{A}_m = D\int_{shell} \dot{w}\boldsymbol{\Delta}\boldsymbol{\Delta} w \,\mathrm{d}s = \frac{\mathrm{d}}{\mathrm{d}t}\left[\frac{1}{2} D\int_{shell}\left(w_{,r^2} + \frac{1}{r} w_{,r}\right)^2 \mathrm{d}s\right], \tag{66}$$

and

$$\dot{E}_{ks} = 2\pi H\rho_d \sum_m^\infty U_m \dot{A}_m \ddot{A}_m = H\rho_d \int_{shell} \dot{w}\ddot{w}\,\mathrm{d}s = \frac{\mathrm{d}}{\mathrm{d}t}\left[\frac{1}{2} H\rho_d \int_{shell} \dot{w}^2\,\mathrm{d}s\right]. \tag{67}$$

The remaining term can be interpreted as a time rate of the coupled kinetic energy of the shell itself

$$\dot{E}_{ksh} = 2\pi H\rho_d \dot{V} \sum_m^\infty O_m^\star \dot{A}_m = H\rho_d \dot{V}\pi R^2 \dot{w}_{mean} = M_{sh}\dot{V}\dot{w}_{mean}, \tag{68}$$

where $M_{sh} = H\rho_d \pi R^2$ is the mass of the shell and $\dot{w}_{mean}$ is the mean deflection velocity of the shell. Finally it is shown that

$$\dot{E}_{jet} + \dot{E}_{kf} + \dot{E}_{ps} + \dot{E}_{ks} = FV + \dot{E}_{ksh}, \tag{69}$$

which formulates the energy conservation law. The numerical accuracy of the energy conservation law is discussed in Ref. [35]. In particular the influence of the ratio M_c/M_{sh} is detailed since the present formulation is based on the assumption of a great value of this parameter.

3. Results and discussion

The parameters which control the phenomena are the thickness H, the initial velocity V_{ini} (alternatively the drop height h_c) and the deadrise angle measured by $T = \tan\beta$. The following scales could be introduced to make the variables non-dimensional: the length scale R, the velocity scale V_{ini} and the scale of the stress E. The resulting time scale is R/V_{ini}. This quantity is much larger than the characteristic time scale of the phenomenon itself, that is to say the interval of time during which the cone is completely wet. As a matter of fact, on the basis of a rigid cone calculation, the duration of the penetration until $a(t) = R$ is of order $R/\dot{a} = O(TR/V_{ini})$ which is much smaller than R/V_{ini} according to the assumption that the deadrise angle is small. On the other hand the elasticity may affect significantly $\dot{a}$, i.e. the velocity at which the wet surface $D(t)$ expands leading to very high values of $\dot{a}$. That is why an additional assumption should be prescribed. The velocity $\dot{a}$ must be much smaller than the sound velocity in water $c_o = 1500$ m/s otherwise acoustic effects may occur.

With a view to comparisons with experimental data by Donguy [17] all the physical parameters will be set to the experimental ones. The experimental set-up had the following characteristics: the outer radius is $R = 0.128$ m, the cone is made of aluminium with a Young's modulus $E = 1.2 \times 10^{11}$ N/m^2, a Poisson coefficient $\nu = 0.3$ and a density $\rho_d = 2700$ kg/m^3. The fluid is water with a density $\rho_f = 1000$ kg/m^3. When the body is free to fall, the mass of the support must be used; in the test this mass $M_c = 30$ kg. The thickness ranges from $H = 0.5$ mm up to $H = 15$ mm, the latter thickness is enough to get an almost rigid shell. The deadrise angle may vary between $\beta = 6^\circ$ and $\beta = 20^\circ$. The drop height ranges from $h_c = 0.9$ m up to $h_c = 3.5$ m.

The main parameter of the present model is the velocity $\dot{a}$ at which the wet body surface expands. It is calculated from the Jacobian (55). It is worth noting that the quantity $[V(t) - \mathbf{Q}(a)\dot{\mathbf{A}}]$ appears in the denominator of the Jacobian and hence may contribute to the time variation of $\dot{a}$. The numerical experiments show that the deflection of the shell evolves so that the first mode only dominates after a minimum of $\dot{a}$ has been reached. It can also be shown that $\mathbf{Q}(a)\dot{\mathbf{A}}$ is always positive. These aspects are discussed in the following developments. First a criterion must be defined to properly choose the necessary number of modes to obtain converged results. The importance of elasticity is discussed. A parametric study shows the influence of each parameter: thickness, deadrise angle and drop height.

3.1. Convergence with the number of modes

The variation of each mode amplitude A_m with m ranging from 1 to 20 is examined. The drop velocity is constant during the penetration into the liquid; it is set to $V_{ini} \approx 8.3$ m/s. The thickness is $H = 1.5$ mm and deadrise angle $\beta = 6^\circ$. The space step Δa is such that $R/\Delta a = 1.28 \times 10^5$. The curves in Figs. 6 and 7 show the variation of the first eight mode amplitudes $(A_m)_{m=1,8}$. The amplitude of the first mode A_1 increases monotonically. This is consistent with experimental observations; the free vibration stage has not started yet (see Ref. [36]). It should be noted that A_m increases significantly at the last stage of the penetration. This can be attributed to the clamping condition of the cone at its outer edge where the structure is very rigid.

The variations of A_m/A_1 with the number of the mode is plotted in Fig. 8 at two stages of the penetration: at mid immersion $a(t)/R = 1/2$ and at complete immersion $a(t) = R$. Knowing that

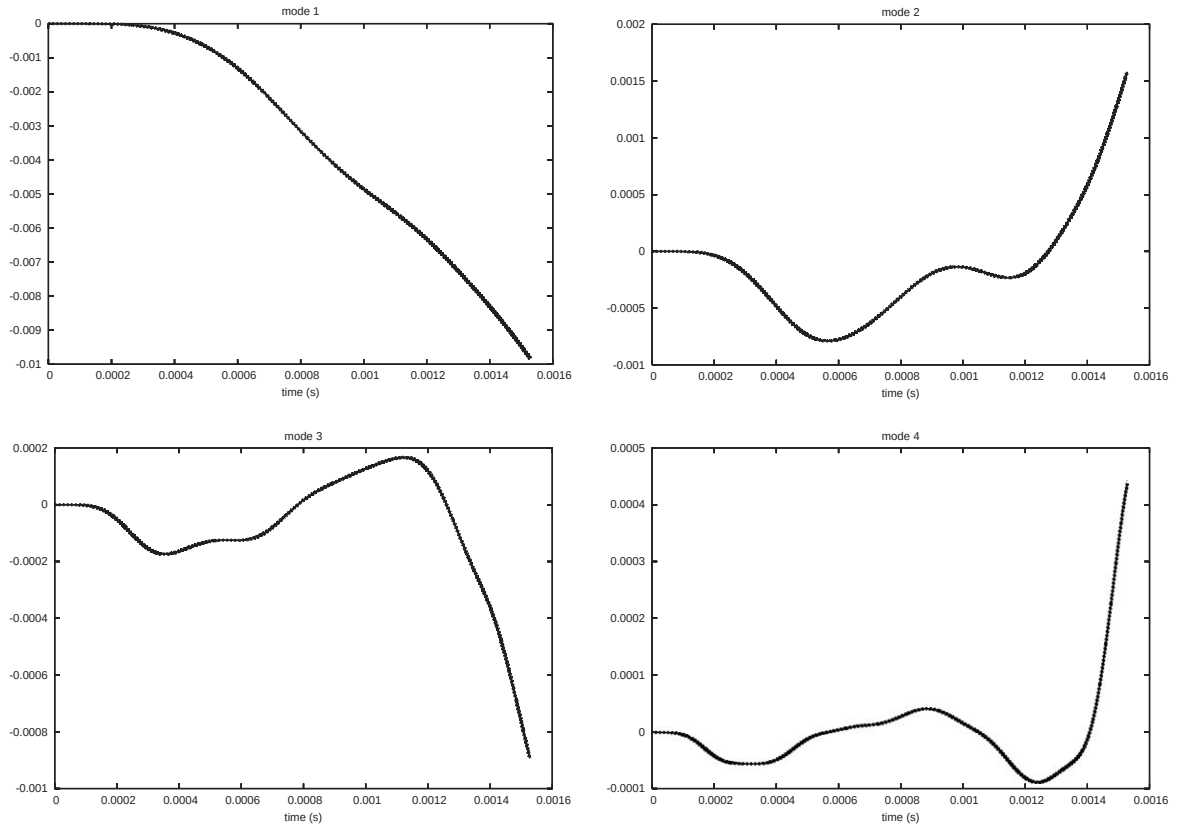

Fig. 6. Time variations of the first eight mode amplitudes $(A_m)_{m=1,8}$ for 4 simulations with a varying total number of modes: either 5 (dotted line), 10 (solid line), 15 (thick solid line) or 20 (thick dotted line) modes. Parameters: constant velocity defined by $V=\sqrt{2gh_c}$ with $h_c=3.5$ m; thickness of the shell $H=1.5$ mm; deadrise angle $\beta=6^\circ$. Numerical integration with space step $R/\Delta a=1.28\times10^5$.

the mode shapes in Eq. (9) all have the same scale (roughly $|w_m(r)|<0.5$), hence A_m is a quantitative indication of each mode contribution. Here it is shown that $A_8/A_1<0.001$ at mid immersion. The deflection is mainly due to the first mode. However the convergence is reached with 10 modes for the present case. To confirm this result, the variations of $a(t)$ and $\dot{a}(t)$ are examined in Fig. 9. Discernable differences only appear at the last stage of the complete immersion in the time series of $\dot{a}(t)$.

In order to evaluate the contribution of moderate-to-high modes, it is usual to correlate the variations of $A_m(t)$ to the variations of the mode shape $w_m(r)$ or to the variations of the quantity $\sigma_m(r)=w_{m,r^2}+\frac{1}{r}w_{m,r}$ which appears in the bending stress (see Ref. [37]). Fig. 10 shows the variations of A_m and w_m with the parameters $a(t)/R$ and r/R respectively. For the present configuration, the deflection and the bending stress vanish at the same nodes but the stress is not defined at the origin $r=0$. The bending stress is not plotted on the figure, but it is known that the variations of $w_m(r)$ and $\sigma_m(r)$ are similar and opposite in sign. At that stage it is not possible to correlate the maxima of $A_m(t)$ and $w_m(r)$ (or $\sigma_m(r)$). On the other hand, it is shown that the contribution of high modes is preponderant at the initial contact but their amplitudes are very

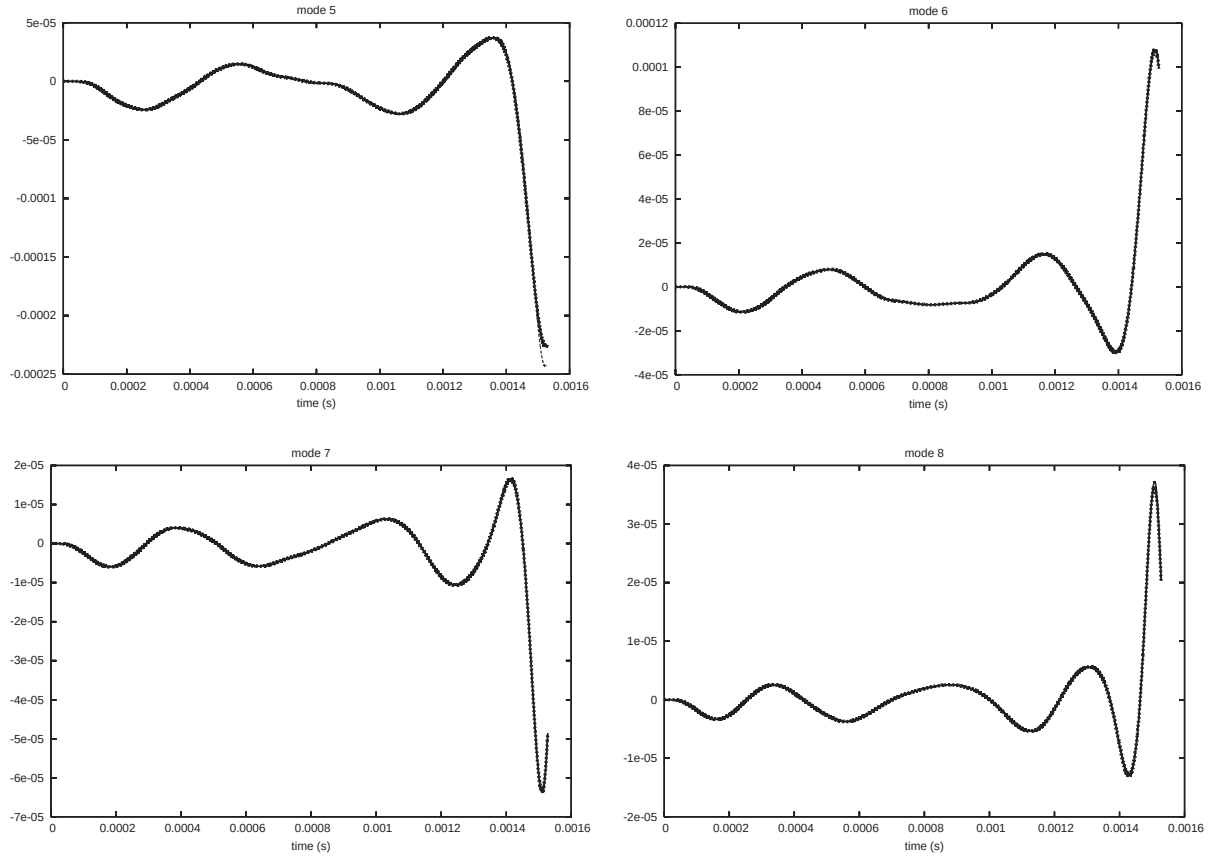

Fig. 7. See caption in Fig. 6.

small. Fig. 11 is a zoom on the variations of A_m from the contact instant up to $a(t)/R = 0.4$ of the immersion. The amplitudes $(A_m)_{m=1,5}$ are made non-dimensional with the amplitude of the first mode calculated at the complete immersion $A_1(a(t) = R)$. It should be noted that the first mode becomes higher than the other modes after one-third of the immersion is reached. In other words, the elastic effects are completely inhibited during the initial stage of the penetration and the deflection mainly occurs close to the contact line during the first stage of immersion.

3.2. *Different stages of the penetration*

Fig. 12 details the different stages of the penetration of the cone for a free-falling cone with a drop height $h_c = 3.5$ m. Two phases are easily identified: before and after the instant when the first mode becomes dominant. This instant will be denoted r_{A_1} instead of the actual corresponding time. Below that point $\dot{a}$ decreases monotonically. The maximum of deflection is tracked in time: it occurs at the position $r = r_{w_{max}}$ along the cone generatrix. The straight line $r = a$ indicates when $r_{w_{max}}$ is below or above the contact point. It is shown that the change occurs at the early stage of penetration. The deflection in fact increases and its maximum occurs close to the contact point, in spite of the fact that the local deadrise angle slightly decreases. The local deadrise angle between

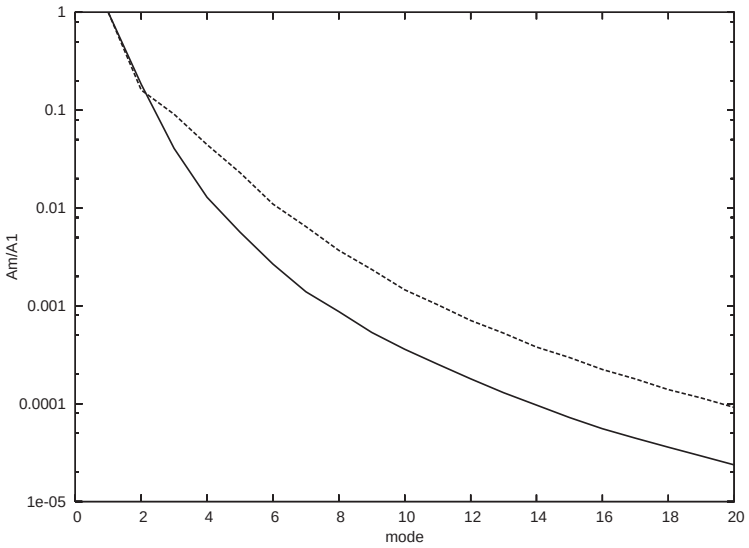

Fig. 8. Variations of A_m/A_1 with the number of the mode at two stages of the penetration: at mid immersion $a(t)/R = 1/2$ (solid line) and at complete immersion $a(t) = R$ (dotted line). Parameters of the simulations: 20 modes and see Fig. 6.

the free surface and the deformed body surface follows from the local slope $\tan\beta^\star = \tan\beta + \partial w(r,t)/\partial r$. During that phase it seems that the maximum deflection and the maximum pressure are rather correlated.

At about $a = r_{A_1}$, there is a stabilization of the maximum deflection, which means that the first mode starts to dominate. Then the immersion accelerates as the local deadrise angle decreases. A maximum is reached before complete immersion, while the local deadrise angle must come back to β. The reason is that the cone is clamped along its outer boundary. The maximum velocity $\dot{a}$ is 2.5 times its initial value. For thinner shells it can be much higher.

After $a = r_{A_1}$, the angle $\beta^\star$ varies significantly. In particular it reaches a negative value before increasing rapidly up to its initial value at complete immersion. The limit $\beta = 4^\circ$ is known to be the lower limit of the linearized Wagner model. This suggests that other phenomena may appear as ventilation. Beyond this point, the standard pressure calculation within potential theory is also questionable. The pressure variation is plotted in Fig. 13. Two points of measurement (P_1, P_2) are identified $r/R \approx 0.31$ and $r/R \approx 0.70$ respectively on both sides of the limit $a(t)/R > 0.55$. One notes that P_2^{max} is about twice P_1^{max}. On the other hand P_2 is divided by a factor 4 within a time interval of 3×10^{-5} s. One can expect that this is too rapid to be caught by any existing sensors. As an example, in experimental measurements, the pressure gauges have a finite dimension: their diameter is about 5 mm long for those used by Donguy [17]. Knowing the speed of the contact line $\dot{a} \approx 100$ m/s, this means that the duration of presence of the peak on the pressure gauge is about $\Delta t \approx 5 \times 10^{-5}$ s. Therefore the measurement of the peak value is quite uncertain as has also been mentioned in Faltinsen [36] in his figure 4. For the same simulation, Fig. 13 also shows the corresponding variations of the penetration, velocity and acceleration with $a(t)$. The velocity undergoes a slight decrease and ends with a default of 4%. The acceleration reaches a maximum value, about 165 times the gravity. To complete this analysis the different components of $\dot{a}$

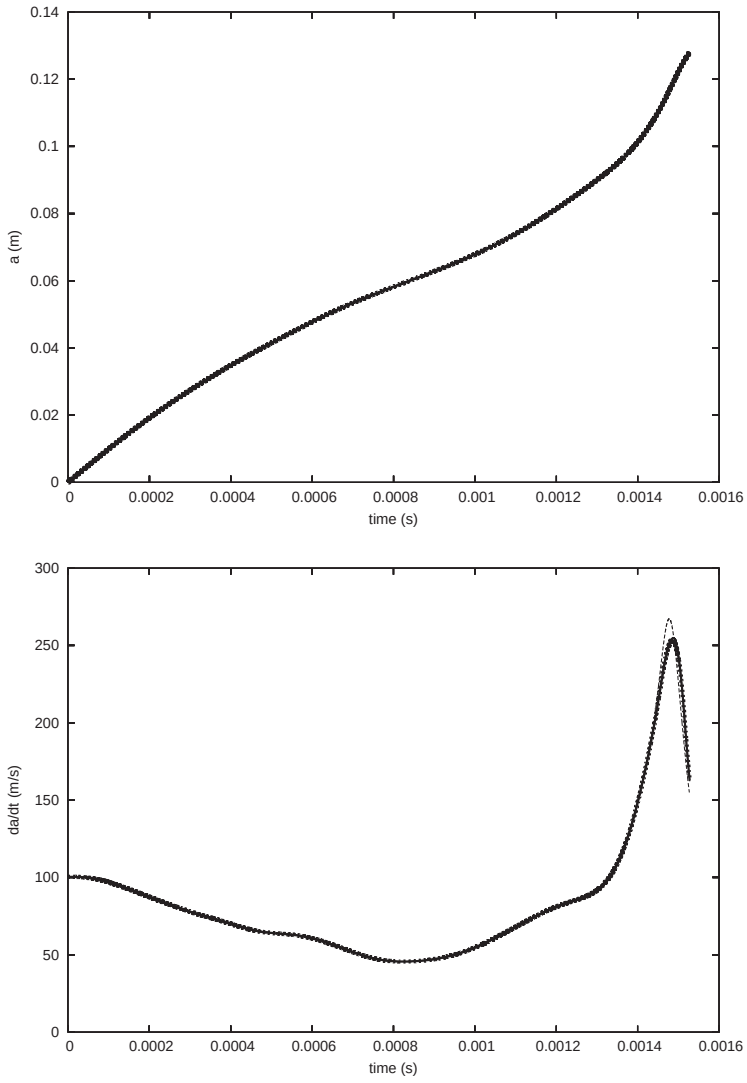

Fig. 9. Time variations of $a(t)$ (top) and $\dot{a}(t)$ (bottom). Parameters of the simulations and nomenclature of the curves: see Fig. 6.

(see Eq. (55)) are plotted in Fig. 14. It is observed that $\dot{a}$ increases as the sum of $\left(\frac{\pi \tan \beta}{4} + \mathbf{Q}'(a)\mathbf{A}\right)$ vanishes. Asymptotically $\dot{a}$ can be very large under these circumstances. On the other hand, $\dot{a}$ can hardly vanish. In fact, for the case illustrated above the initial velocity is $V_{ini} \approx 8.28$ m/s and it is much larger than the maximum value of $\mathbf{Q}(a)\dot{\mathbf{A}}$.

3.3. Importance of the elasticity

The importance of the elasticity effects can be quantified with respect to the rigid case. For the same parameters used in the previous sections, Fig. 15 shows the time variations of the velocity

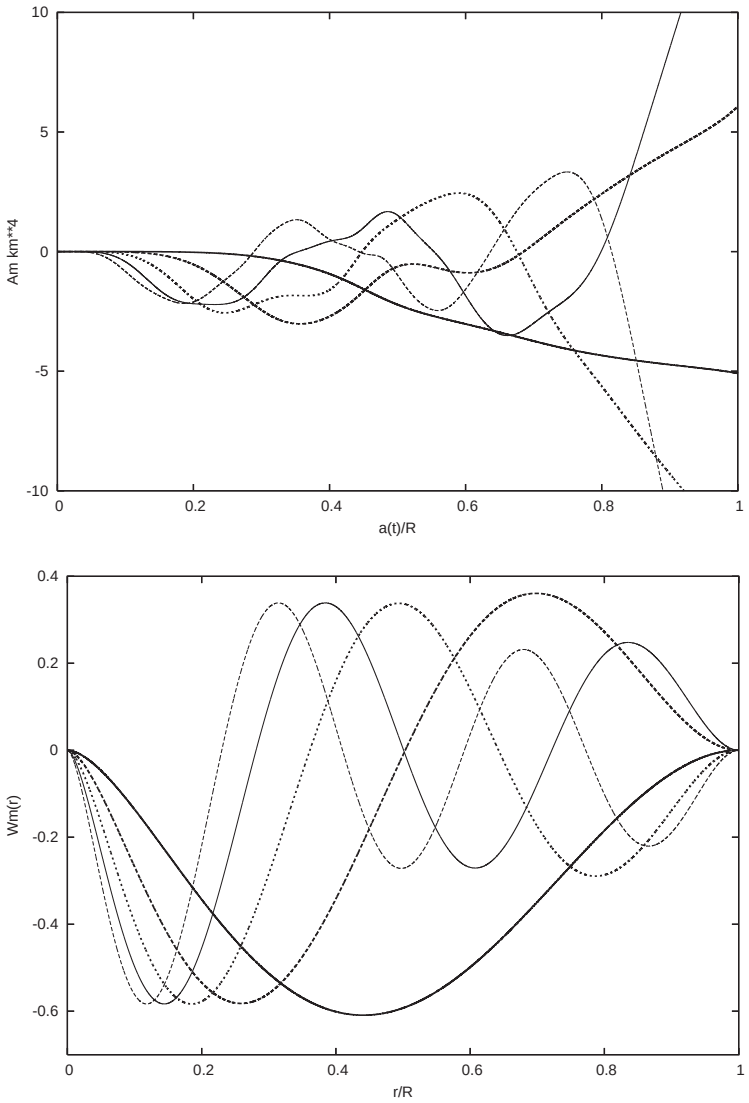

Fig. 10. Variations of $A_m k_m^4$ (top) and w_m (bottom) with the parameters $a(t)/R$ and r/R respectively. Parameters of the simulations: 20 modes and see Fig. 6. Mode 1: thick solid line, mode 2: thick dashed line, mode 3: thick dotted line, mode 4: thin solid line, mode 5: thin dashed line.

and acceleration up to complete immersion. The differences are noticeable not only on the amplitude but also on the duration of the simulation. A comparison of the velocity at the time instant where the cones (rigid or elastic) are completely immersed shows that

$$\left|\frac{V_{rigid} - V_{elastic}}{V_{rigid}}\right| \approx 5\% \quad \left|\frac{\dot{V}_{rigid} - \dot{V}_{elastic}}{\dot{V}_{elastic}}\right| \approx 18\% \tag{70}$$

Up to 80% of immersion of the elastic cone, its acceleration is much lower than the acceleration of the rigid cone. However at complete immersion of the elastic cone the acceleration (and

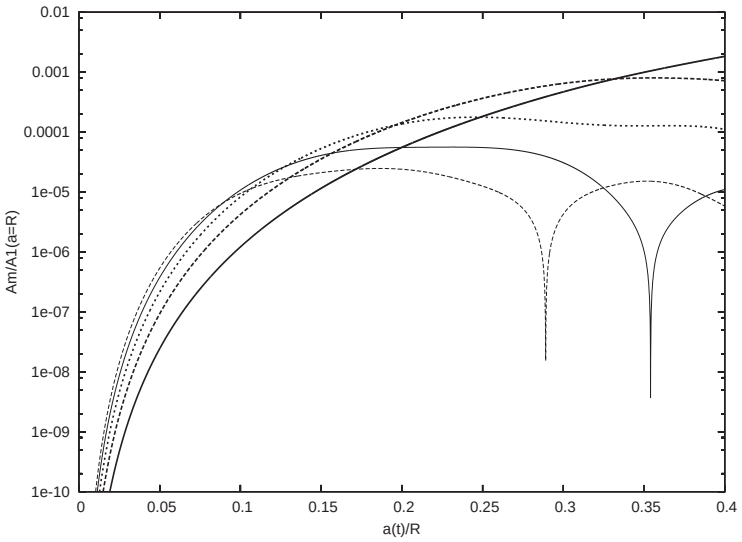

Fig. 11. Zoom on the variations of A_m with the parameter $a(t)/R$ from the initial contact instant up to $a(t)/R = 0.4$ of the immersion. The logscale is used in the vertical coordinate, and the variations of $\log|A_m/A_1(R)|$ are actually plotted where $A_1(R)$ is the amplitude of the first mode at complete immersion $a(t) = R$. The cusps correspond to zeroes of A_m. Mode 1: thick solid line, mode 2: thick dashed line, mode 3: thick dotted line, mode 4: thin solid line, mode 5: thin dashed line.

consequently the force) reaches a higher value than for the rigid cone. This is due to the clamping condition along the edge of the cone. For the pressure measured at the two points $r/R \approx 0.31$ and $r/R \approx 0.70$ along the generatrix of the cone, their variations with $a(t)/R$ are plotted in Fig. 16. The relative amplitudes of the pressure peaks at points 1 and 2 between the rigid and elastic are inverted. The variations of the pressure after the peak also show a clear difference of amplitude; there is a factor greater than 2. The difference of the peak amplitude is explained by comparing the time variations of $\dot{a}$ (also plotted in Fig. 16) since the peak is proportional to $\dot{a}^2$.

3.4. Parametric study

It appears that the velocity at which the wet surface expands is strongly affected by the elastic characteristics of the shell. This parameter has been chosen to discuss the parametric influence of the shell thickness, drop height and deadrise angle, on the main features of the phenomenon.

3.4.1. Influence of the shell thickness

The time variation of $\dot{a}$ with the thickness is quite noticeable. It is illustrated here for free drop tests. With two drop heights $h_c = 0.90$ m, $h_c = 3.50$ m and deadrise angle $\beta = 6^\circ$, the thickness varies in the range $H \in [1\text{ mm} : 15\text{ mm}]$. The results are illustrated in Figs. 17 and 18, where two series of "small" and "large" thicknesses are compared in terms of the time variation of $\dot{a}$. It appears that the interval $H \in [2\text{ mm} : 5\text{ mm}]$ is a transition between two behaviours: rigid-like and elastic-like. For small thicknesses the duration of the immersion increases significantly and the clamping condition at the outer edge strongly affects the kinematics of the drop before complete

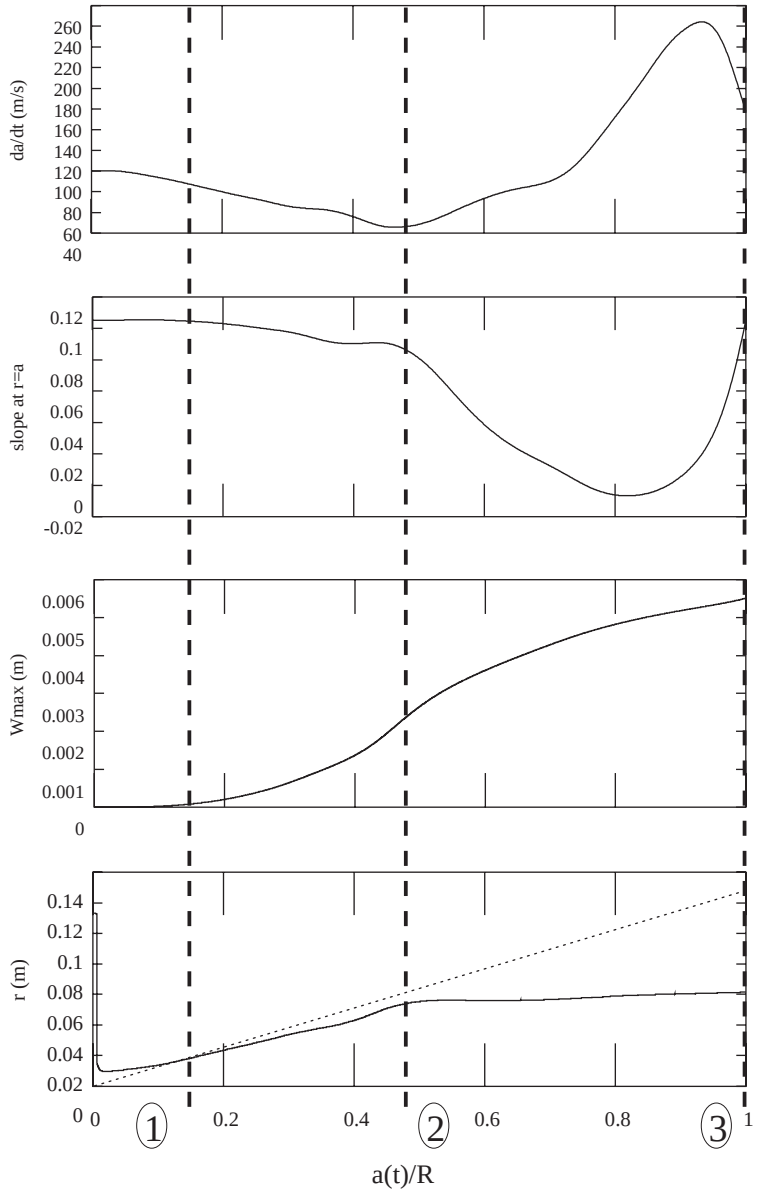

Fig. 12. Different stages of the penetration during a free falling cone with a drop height $h_c = 3.5$ m. From top to bottom: (i) velocity of the expanding wetted surface $\dot{a}$, (ii) local deadrise angle between the free surface and the deformed body surface $\tan\beta^{\star} = \tan\beta + \partial w(r,t)/\partial r$, (iii) maximum of deflection w_{max}, (iv) position (solid line) along the cone generatrix of the maximum of deflection $r = r_{w_{max}}$ relatively to the contact line $r = a(t)$ (dashed line). Surrounded numbers (1): instant when $r_{w_{max}}$ is below or above the contact point, (2): instant $a = r_{A_1}$ when the first mode gets dominant, (3): instant of complete immersion.

immersion. In the transition range, the monotony of $\dot{a}$ changes. Whatever the thickness, the velocity of penetration $V(t)$ always decreases monotonically. Its final value at $a(t) = R$ (non-dimensional with the initial velocity V_{ini}) is plotted in Fig. 19 as the thickness varies. It is worth

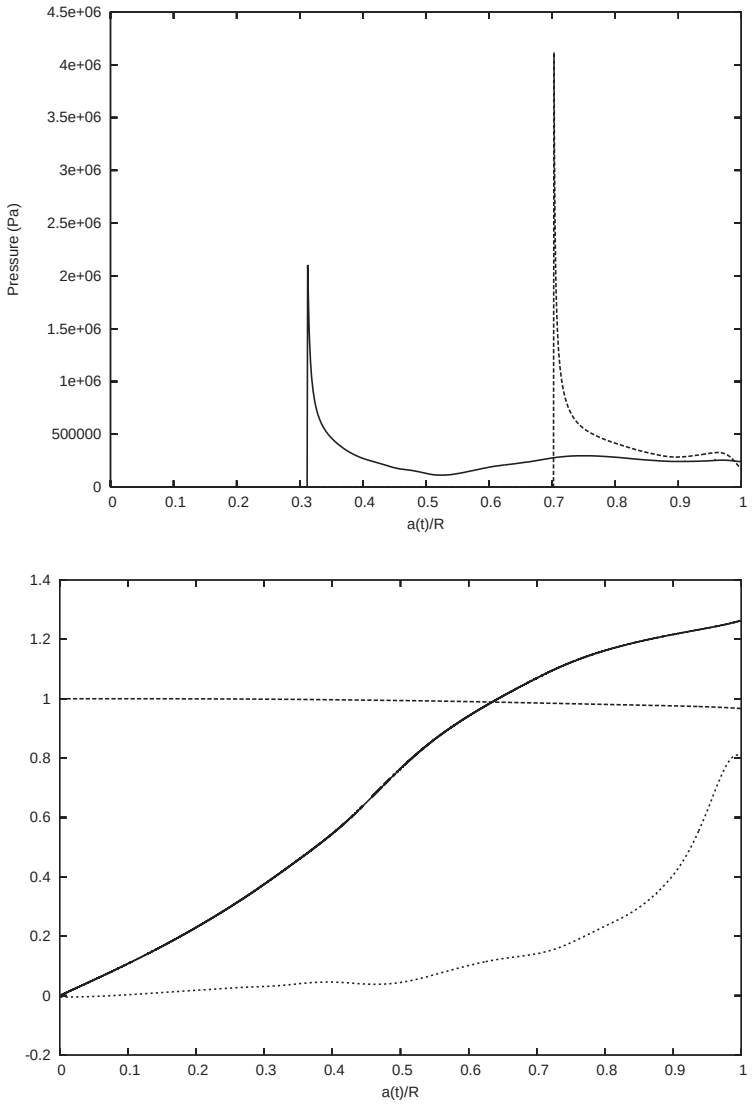

Fig. 13. Top: Pressure variation with $a(t)$ at two points $r/R \approx 0.31$ (solid line) and $r/R \approx 0.70$ (dotted line). Bottom: Variations with $a(t)$ of the penetration depth $h(t)$ (solid line) made non-dimensional with factor 100, velocity $V(t)$ (dashed line) made non-dimensional with initial velocity and acceleration $\dot{V}(t)$ (dotted line) made non-dimensional with factor -2000. Parameters: see Fig. 12.

noting that the decline of the velocity increases with the thickness. This means that elasticity makes the velocity more constant during penetration. The higher the initial velocity, the more elastic the shell, the more constant the velocity of penetration.

3.4.2. Description of the cavity formation

Two stages of the cone deflection are shown in Fig. 20 up to the instant when an entrapped air pocket is formed. In the present approach, the simulation is stopped unless a secondary contact

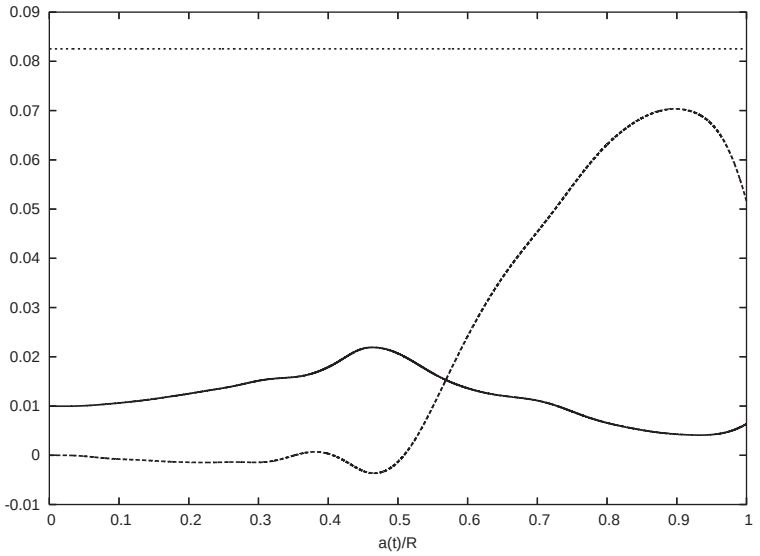

Fig. 14. Variations of different components with $a(t)/R$. These terms appear in $\dot{a}$ as defined in Eq. (55): $\pi \tan \beta/4$ (dotted line), $-\sum_m A_m(t)Q'_m(a)$ (dashed line) and $\sum_m \dot{A}_m(t)Q_m(a)$ (solid line). Parameters: see Fig. 12.

point can be accounted for. This means that the local configuration close to the new contact point must be identified. This is quite feasible within the linearized Wagner technique (see Ref. [13]) as long as the main hypothesis of small deadrise angle is not violated. However, one can also expect that the phenomena which occur in the air cavity are far from simple. For example, part of the fluid evacuated in the jet is certainly entrapped in the cavity as well. Hence the usual hypothesis of constant pressure in the cavity is questionable.

The formation of the cavity can be anticipated by examining the configuration where the free surface deformation is such that the outer edge gets wet. This time instant follows from the geometric identity

$$\eta(R,t) + h(t) = R \tan \beta. \tag{71}$$

It is reasonable to assume that the first mode dominates, hence the free surface elevation calculated from Eq. (29) yields an expression of the first mode amplitude as a function of a and the penetration depth h

$$A_1(a,h) = \frac{\pi}{2E_1}\left[h\left(1\frac{2}{\pi}\mathrm{Y}_2(R/a)\right) - R\tan\beta - \frac{a\tan\beta}{2}\mathrm{Y}_3(R/a)\right]. \tag{72}$$

The limiting stress of the shell is about $\sigma_{elas} \approx 350$ MPA. The corresponding limiting amplitude A_1 is given by

$$(A_1)_{elas} = \frac{\sigma_{elas}}{E\sigma_1^{max}}, \tag{73}$$

where σ_1^{max} is the maximum value of the stress along a generatrix of the cone and E is the Young's modulus. From a parametric study which is not detailed here, it appears that there is a non-negligible area (a,h) where the cavity might be formed.

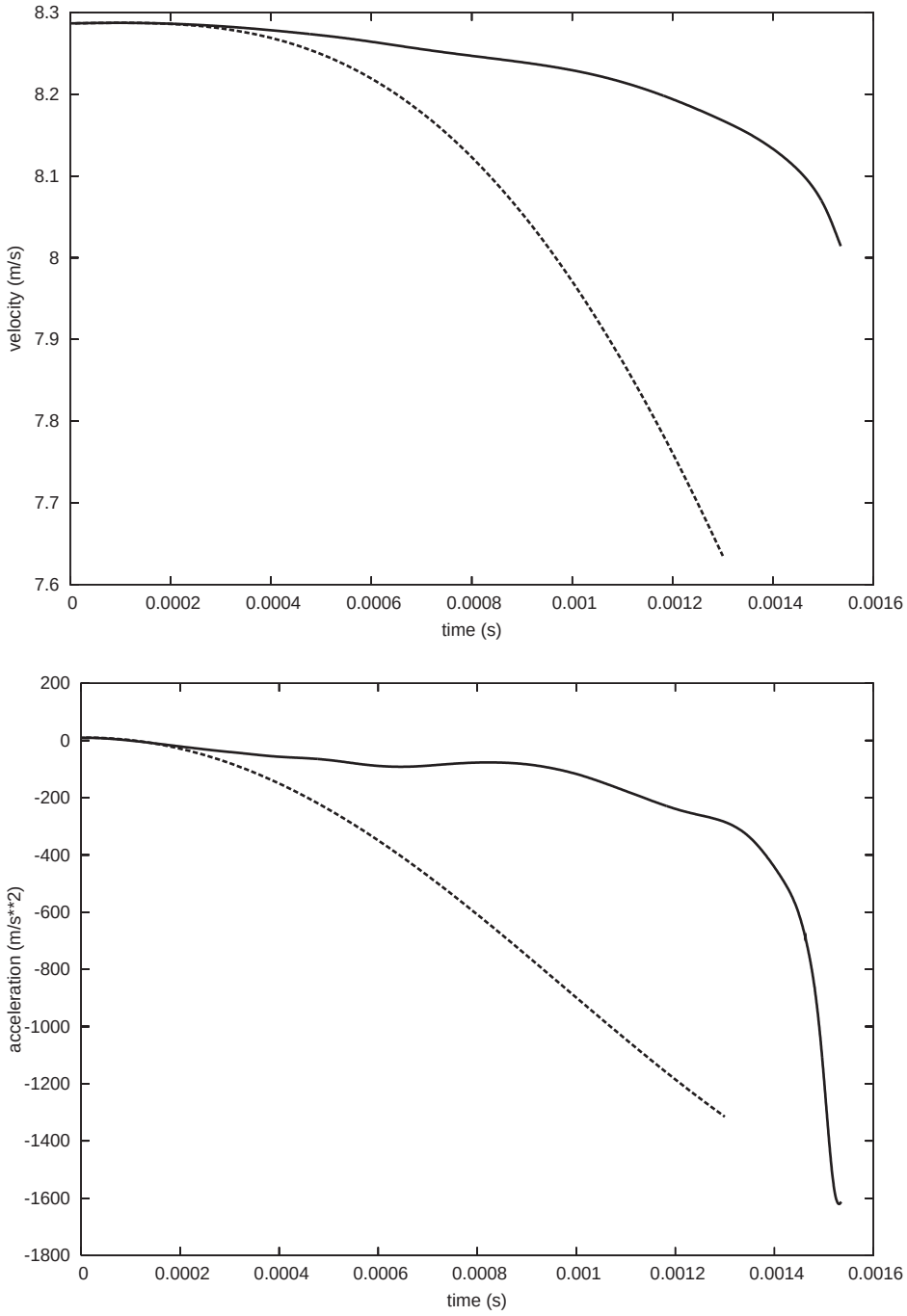

Fig. 15. Comparison between elastic (solid line) and rigid (dashed line) cones. Time variations of the velocity (top) and acceleration (bottom) up to the complete immersion. Parameters: drop height $h_c = 3.5$ m, deadrise angle $\beta = 6^\circ$ and thickness $H = 1.5$ mm.

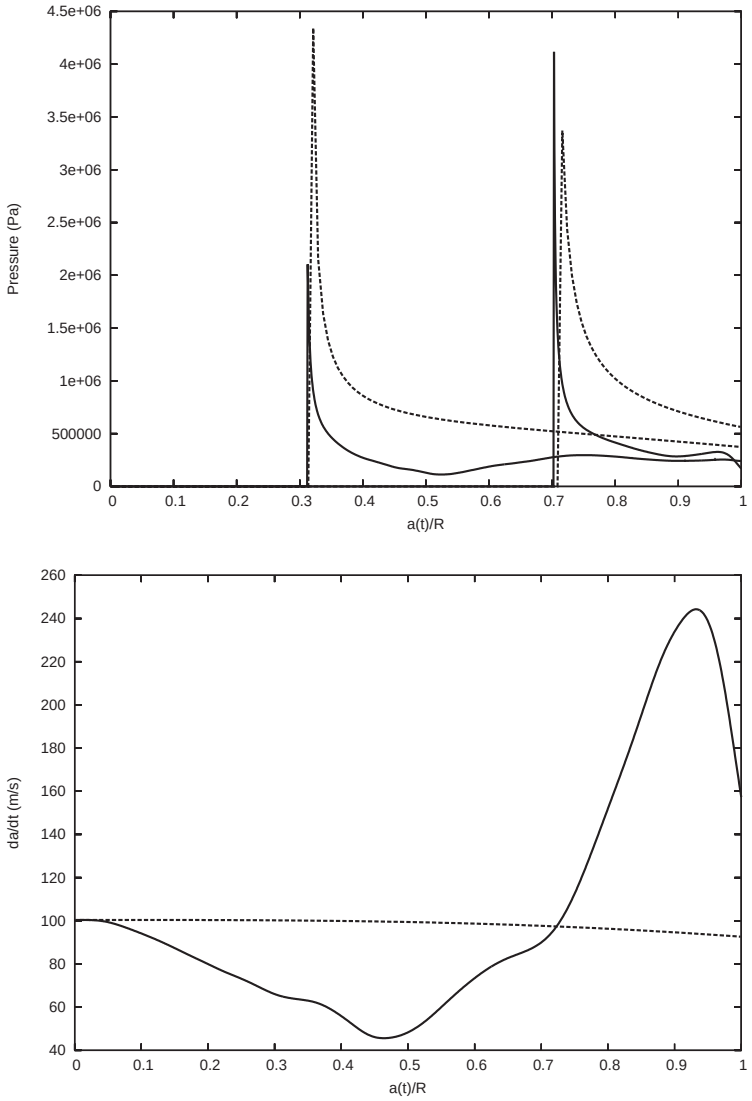

Fig. 16. Comparison between elastic (solid line) and rigid (dashed line) cones. Variation of the pressure (top) measured at the two points $r/R \approx 0.31$ and $r/R \approx 0.70$ as a function of $a(t)/R$. Variation of $\dot{a}$ (bottom) in terms of $a(t)/R$. Parameters: see caption in Fig. 15.

3.4.3. *Influence of the deadrise angle*

The deadrise angle is allowed to vary between $\beta = 6^\circ$ up to $\beta = 20^\circ$ with the increasing step 1°. The higher value is known to be the upper allowed limit of the Wagner theory. Considering the thickness $H = 1.5$ mm, Fig. 21 illustrates the time variation of $\dot{a}$ for the studied angles β. For lower thicknesses and low values of β unphysical results are obtained. The velocity $\dot{a}$ may reach the threshold defined by the sound velocity in water. Acoustic effects may occur and the present

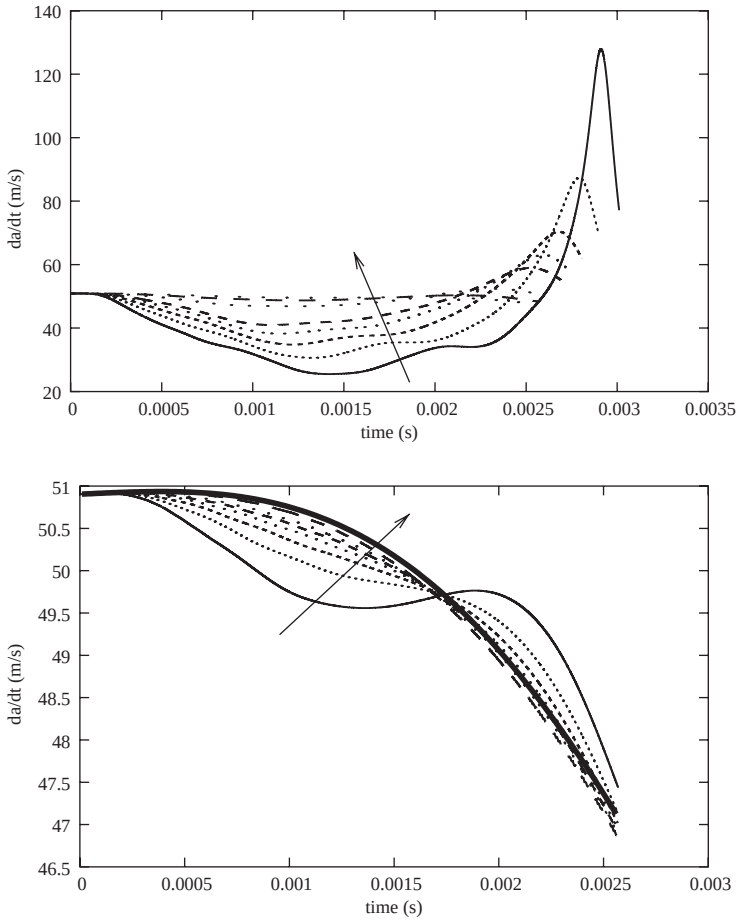

Fig. 17. Time variations of $\dot{a}$ for free drop tests with drop height $h_c = 0.90$ m and deadrise angle $\beta = 6^\circ$, Top: the thickness varies in the range $H \in \{1; 1.25; 1.5; 1.75; 2; 3; 4; 5\}$ in millimeters. Bottom: the thickness varies in the range $H \in \{5; 6; 7; 8; 9; 10; 15\}$ in millimeters. The arrow indicates the increasing thickness. The time variation of $\dot{a}$ for a rigid cone is also plotted (thick solid line).

approach fails. Progressively, for larger deadrise angles the monotony of $\dot{a}$ becomes very smooth. Fig. 21 shows the deflection measured at the $r/R \approx 0.31$. It is not the maximum deflection of the shell and hence it can be expected that much larger deflections can be obtained for a shell which is flatter and thinner. It should be noted that for the present computations, there is a critical angle beyond which a cavity is formed; it is $\beta = 12^\circ$.

3.4.4. Influence of the drop height

An increasing drop height h_c implies not only faster immersion but also amplification of the elastic effects. The influence of h_c is more or less identical to what has been already observed. Fig. 22 illustrates the time variations of $\dot{a}$ for drop heights ranging from $h_c = 90$ cm up to $h_c = 350$ cm. The deadrise angle is $\beta = 6^\circ$. A low thickness

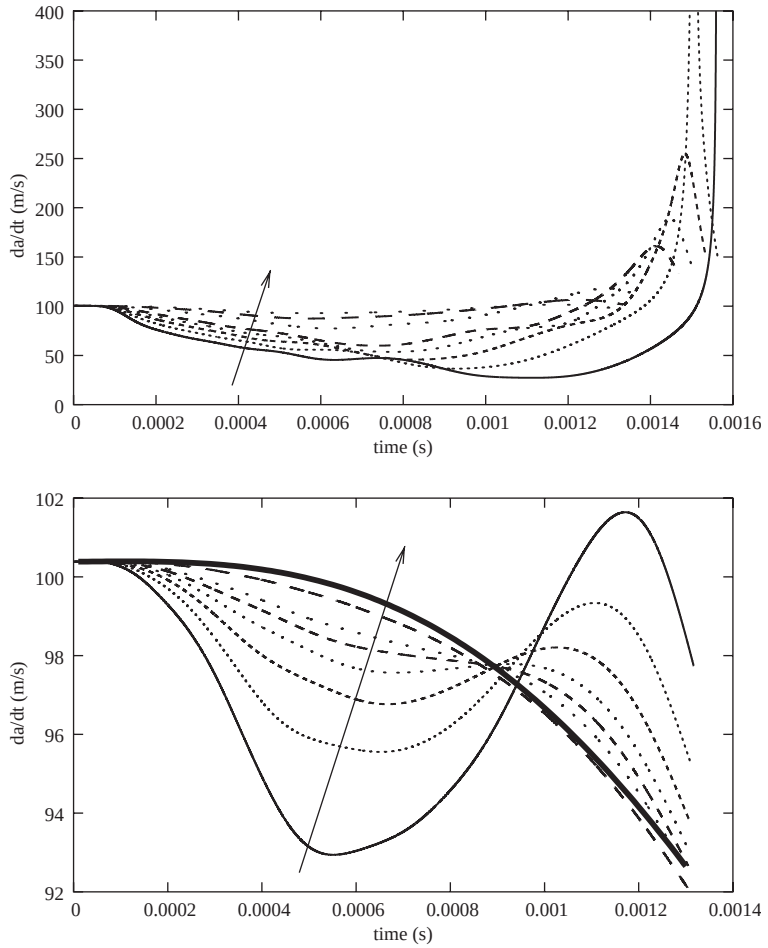

Fig. 18. Time variation of $\dot{a}$ for free drop tests with drop height $h_c = 3.50$ m. See notations in the caption of Fig. 17.

($H = 0.5$ mm) leads to the formation of a cavity with unphysical deflection amplitudes. For greater thicknesses (the curves correspond to thickness $H = 1.5$ mm), the effects of elasticity are still non-negligible. Finally for a "high" thickness $H = 5$ mm, the variations of the deflections show that a maximum is reached before complete immersion and it is expected that free vibrations may start.

3.4.5. Energy conservation

The energy conservation law is formally proved in the theoretical developments in Section 2.4 and it is checked numerically. The numerical accuracy mainly depends on the total number of modes of the modal decomposition. To a lesser extent, it also depends on the numerical integration of system (56). First the time variation of different components is examined in Fig. 23: the velocity of expansion $\dot{a}$, the velocity of penetration $V(t)$ and the quantity $\mathbf{Q}(a)\dot{\mathbf{A}}$ which

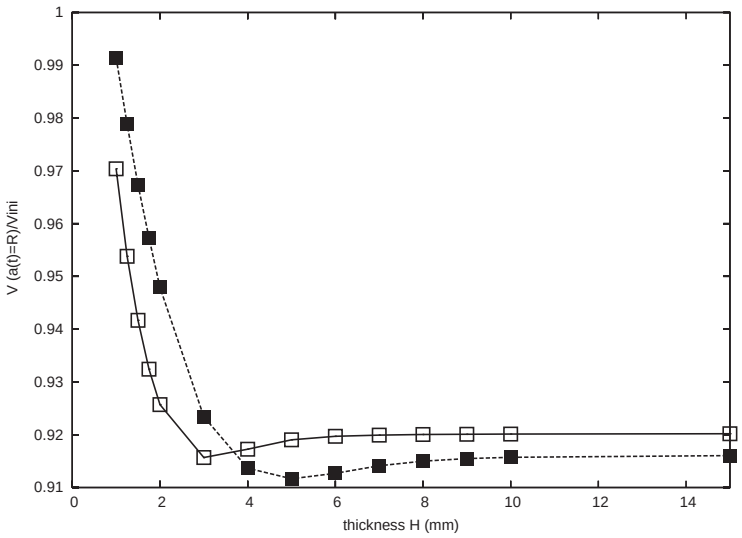

Fig. 19. Variation of the velocity at complete immersion ($a(t) = R$) in terms of the thickness H. The velocity is made non-dimensional with the initial velocity V_{ini}. Two drop heights are considered: $h_c = 0.90$ m (empty square) and $h_c = 3.50$ m (filled square).

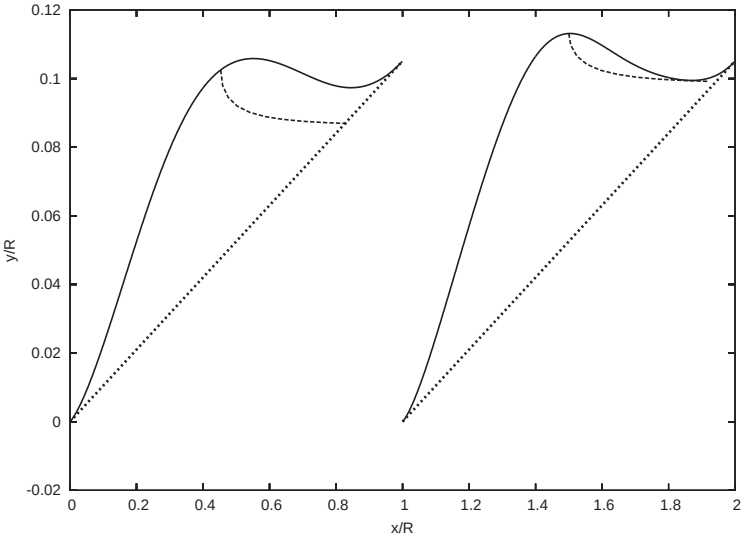

Fig. 20. Two stages of the cone deflection (solid lines) at time instants $t \approx 0.00262$ s (left), and $t \approx 0.00299$ s (right). The free surface is plotted with dashed line and the undeformed cone with dotted line. A cavity is formed at the second stage and consequently the simulation stops.

quantifies the elasticity effects. The following non-dimensionalization formulas are used:

$$\delta_{nodim} = \frac{32\delta}{RT^2}, \quad \dot{a}_{nodim} = \frac{\dot{a}}{\dot{a}_{ini}}, \quad V_{nodim} = \frac{V(t)}{V_{ini}}, \quad [\mathbf{Q}(a)\dot{\mathbf{A}}]_{nodim} = \frac{\mathbf{Q}(a)\dot{\mathbf{A}}}{V_{ini}}, \tag{74}$$

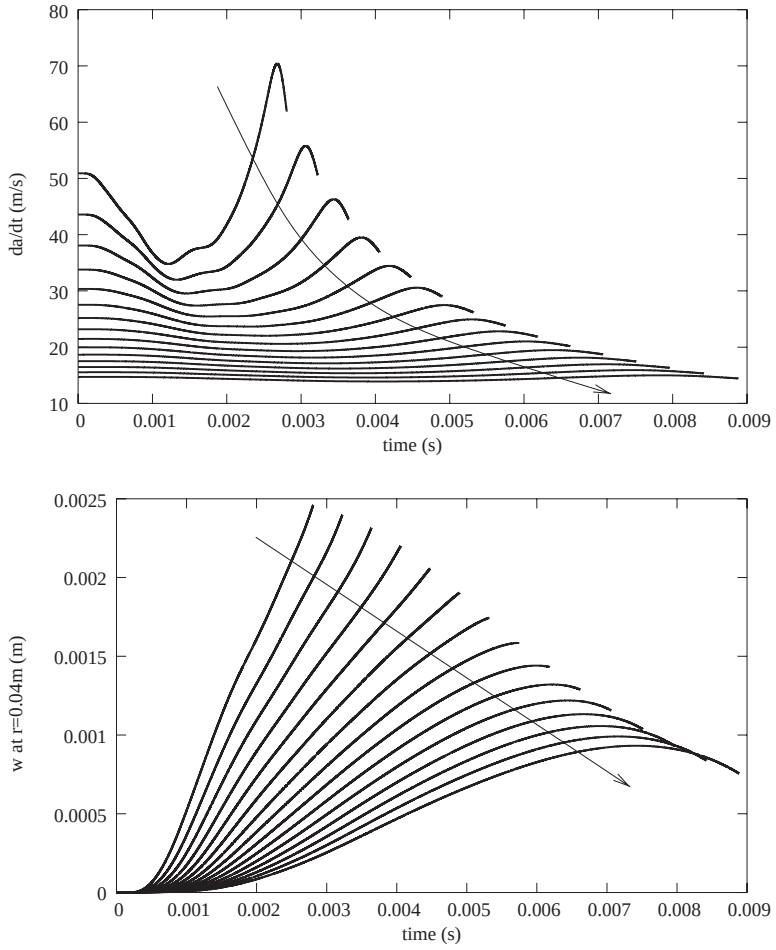

Fig. 21. Top: Time variations of $\dot{a}$ for deadrise angles ranging from $\beta = 6^\circ$ up to $\beta = 20^\circ$ with step 1°. Parameters: thickness $H = 1.5$ mm, drop height $h_c = 0.9$ m. Bottom: corresponding time variations of the deflection calculated at point $r/R \approx 0.31$. The arrow indicates the increasing deadrise angle.

and the ratio of the "elastic" jet thickness to the "rigid" jet thickness[4] is

$$\frac{\delta_{elastic}}{\delta_{rigid}} = \left(\frac{V - \mathbf{Q}(a)\dot{\mathbf{A}}}{V}\right)^2, \quad \delta_{rigid} = \frac{a}{2\pi\dot{a}^2} V^2. \tag{75}$$

The quantity $\mathbf{Q}(a)\dot{\mathbf{A}}$ is always positive. To a certain extent, it can be interpreted as a measure of the elasticity effects. This term appears in the jet thickness δ and in the Jacobian $\mathrm{d}t/\mathrm{d}a$. It peaks with the minimum of $\dot{a}$ and the maximum of δ. For the present calculation the maximum jet thickness is $\delta_{max} \approx 72$ μm and the corresponding velocity of the fluid in the jet is $V_f = 2\dot{a} \approx 100$ m/s. The time variation of these quantities can be correlated to the time variations of

[4] This quantity is abusively referred to as "rigid" since $\dot{a}$ is the velocity of expansion of the elastic cone and not the computed one for the rigid cone.

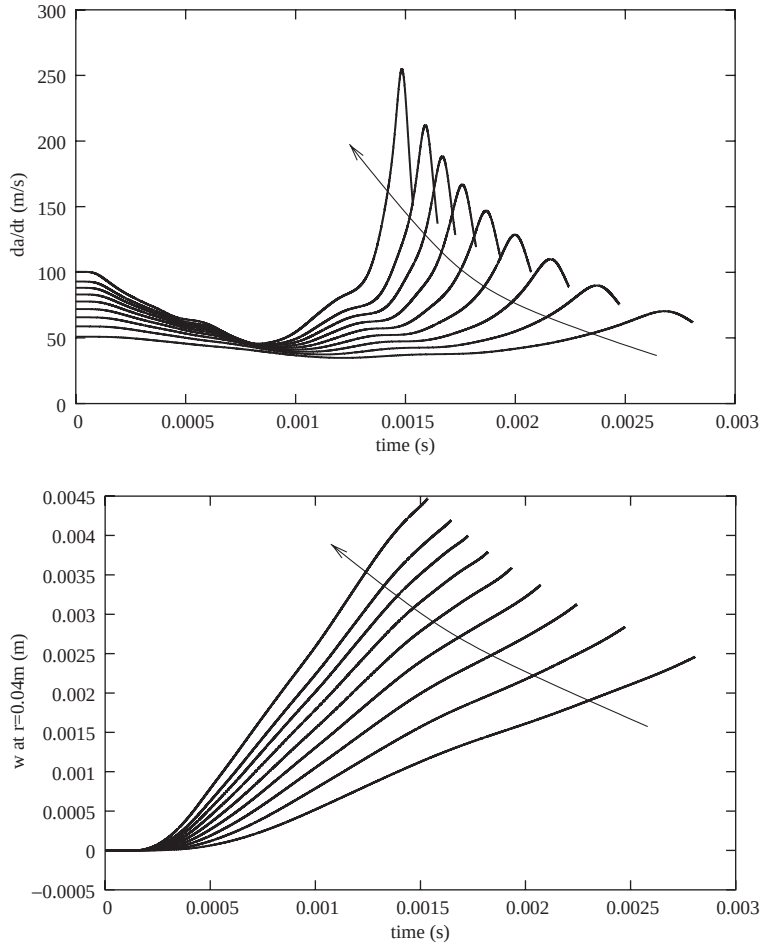

Fig. 22. Top: Time variations of $\dot{a}$ for drop height ranging from $h_c = 90$ cm up to $h_c = 350$ cm. Parameters: thickness $H = 1.5$ mm, deadrise angle is $\beta = 6^\circ$. Bottom: corresponding time variations of the deflection calculated at point $r/R \approx 0.31$. The arrow indicates the increasing drop height.

energies. The different components of the energies are plotted in Fig. 24. Among the different components, the variation of the kinetic energy of only the elastic shell is non-monotonic. This component peaks when the thickness of the jet is maximum in spite of the fact that the velocity of the fluid in the jet reaches precisely its minimum there. The kinetic energy evacuated in the jet and the energy transmitted to the bulk of the fluid have comparable magnitudes. This is consistent with the rigid case and the fact that the velocity of penetration is almost constant. At mid-immersion, the first mode dominates and the corresponding deflection increases monotonically. As a consequence the potential energy of the shell also increases and becomes higher than the other components. In order to quantify the importance of the first mode relatively to higher modes, Fig. 25 shows the total potential energies of the shell and its restriction to the first mode. It may be seen that most energy (70% of the total potential energy) originates from the first mode. This quantifies the error which occurs by using the first mode approximation.

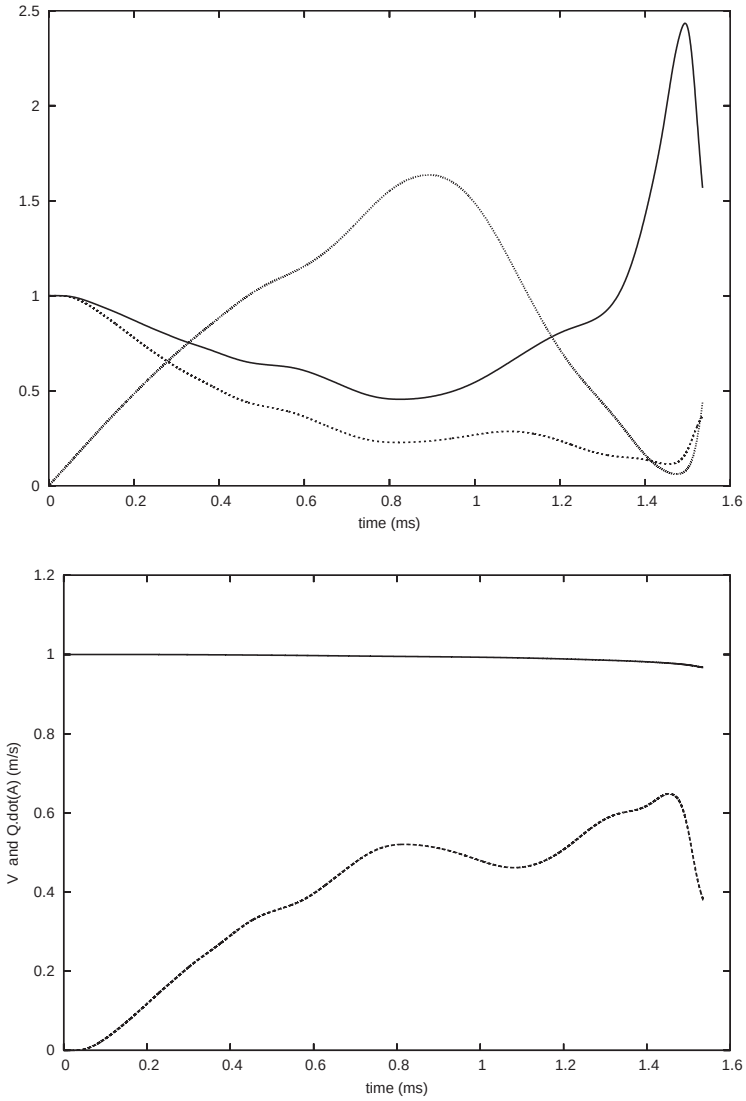

Fig. 23. Time variations of different components characterizing the jet. These quantities are made non-dimensional according to Eqs. (74) and (75). Top: velocity of expansion $\dot{a}$ (solid line), jet thickness δ (dashed line) and jet thickness ratio $\delta_{elastic}/\delta_{rigid}$ (dotted line) between rigid and elastic case. Bottom: velocity of penetration $V(t)$ (solid line) and quantity $\sum_m \dot{A}_m(t)Q_m(a)$ (dashed line) appearing in jet thickness. Parameters: thickness $H = 1.5$ mm, drop height $h_c = 3.5$ m and deadrise angle $\beta = 6^\circ$.

3.4.6. Pressure distribution

Comparisons with experimental data are done for the pressure distribution. The experimental set-up is described in Donguy [17]. Two points of measurements are identified along a generatrix of the cone at $r/R \approx 0.3$ and $r/R = 0.7$ from the apex.

In Fig. 26, the time variations of the pressure are plotted for a deadrise angle $\beta = 14^\circ$ and a thickness $H = 1.5$ mm. The velocity at the initial contact point is $V_{ini} = 2.5$ m/s. The comparisons

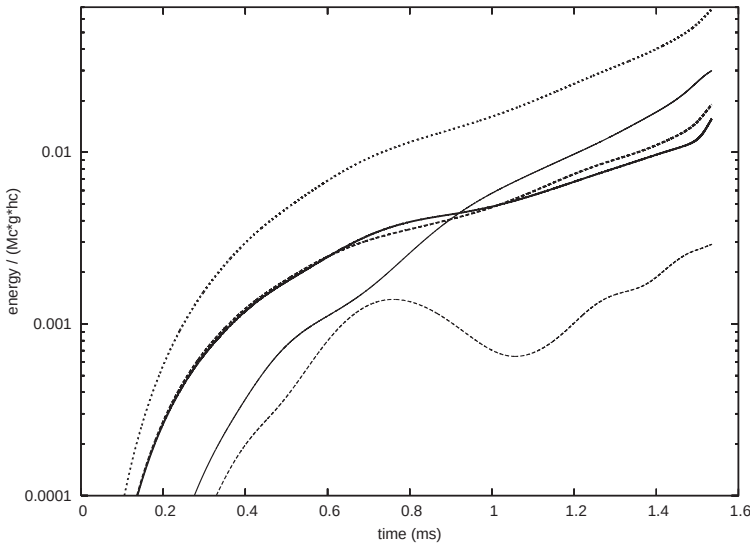

Fig. 24. Time variations of the different energies components made non-dimensional with the initial kinetic energy at the contact instant $\gamma M_c h_c = \frac{1}{2} M_c V_{ini}^2$. Components: shell potential energy (thin solid line), shell kinetic energy (thin dashed line), fluid kinetic energy (thick solid line), kinetic energy in the jet (thick dashed line), work of the impact force (thick dotted line).

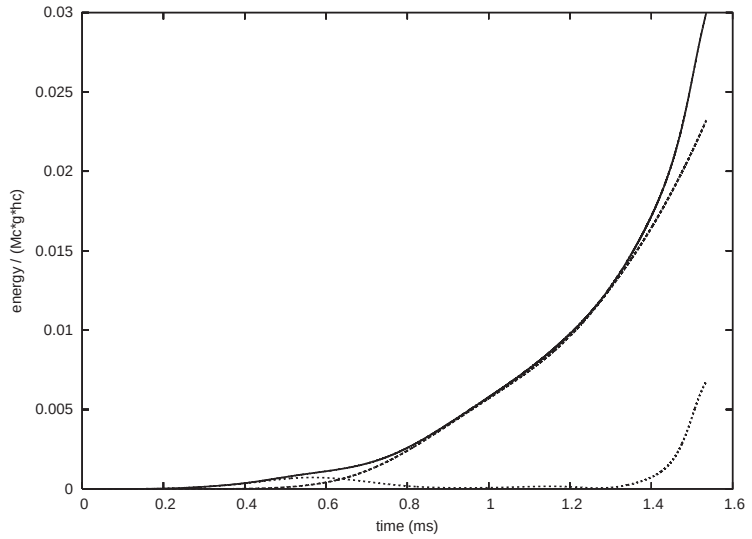

Fig. 25. Time variations of the total potential energies of the shell and its restriction to the first mode. Non-dimensionalization with $\gamma M_c h_c$. Total potential energy: solid line, potential energy mode No. 1: dashed line, difference (total—mode No. 1): dotted line.

are adjusted so that the pressure maxima appear at the same instant. This is justified at least for the first wet pressure gauge, since a common origin in time is necessary. For the second pressure gauge this is questionable but the time interval for adjustment is indicated in the figure just below

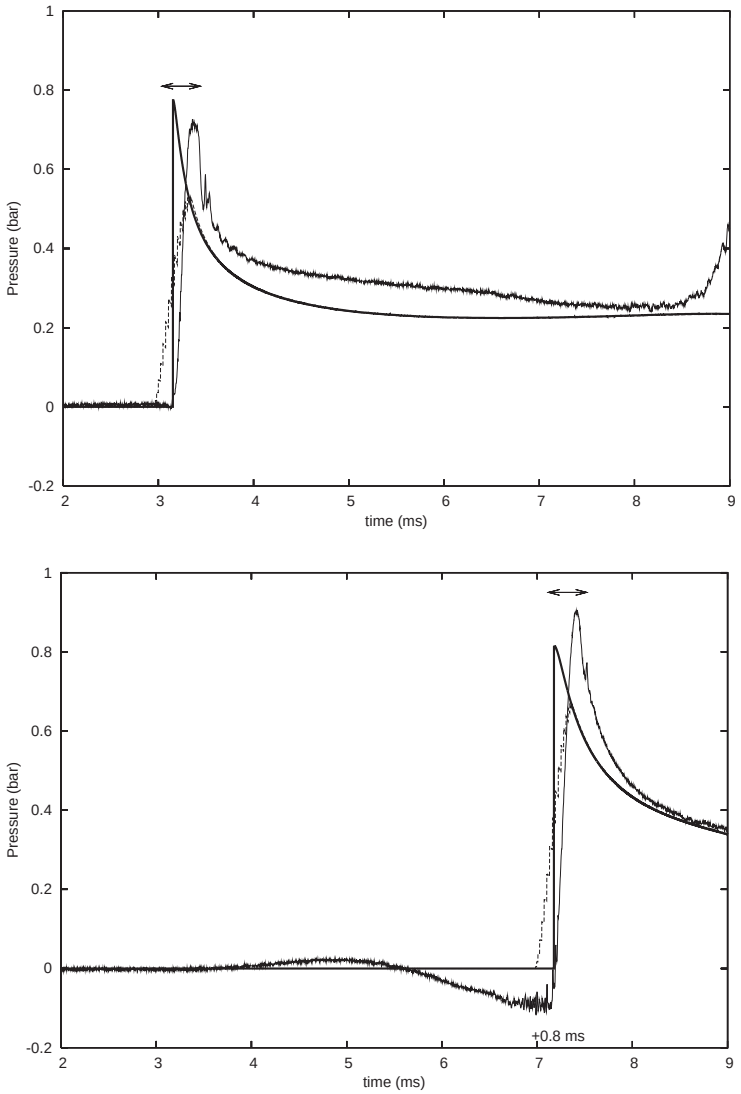

Fig. 26. Comparison between experimental and numerical time variations of the pressure calculated or measured at the points $r/R \approx 0.3$ (top) and $r/R = 0.7$ (bottom). Pressure exactly at the point of measurements: thick solid line, pressure averaged over the surface of the pressure gauge: thin dashed line, experimental results: thin solid line. The arrow shows the duration of the ramp in the numerical simulation. The figure +0.8 ms below the second peak pressure (lower figure) is the time interval for adjustment to approximately superpose the ramp. Parameters: deadrise angle $\beta = 14^\circ$, thickness $H = 1.5$ mm. initial velocity $V_{ini} = 2.5$ m/s.

the second pressure peak. Different reasons can be invoked for this discrepancy (even small). One is the non-colinearity of the drop axis and the symmetry axis of the cone.

Another discrepancy concerns the ramp for which the pressure reaches its maximum. The surface of the pressure gauge in contact with water is circular with diameter 5 mm. Knowing also $\dot{a}$ the velocity of expansion of the wet surface—this is also the velocity at which the pressure peak

moves—provides a ramp duration ranging from 0.2 to 0.45 ms depending on the parameters. A small arrow is hence drawn above each pressure peak. A better comparison of the pressure is thus shown by averaging the pressure distribution over the gauge surface. This allows the ramp to be reproduced but it may also lead to a substantial reduction of the pressure peak.

The experimental results reveal several phenomena that are not reproduced by the model. For example the pressure may decrease before the peak passes through the pressure gauge. This was also observed for rigid body and other experimental campaigns (see Ref. [38]). Ventilation effects might occur there.

4. Conclusions

The present coupled hydroelastic approach shows that the elasticity strongly affects the behaviour of an elastic shell, compared to the rigid case. The structural problem is posed in terms of a modal formulation of the deflection through a linear model for thin shells. The hydrodynamic problem is posed within the frame of the linearized Wagner theory and provides the hydrodynamic pressure distribution acting on the shell.

The critical parameter is the velocity at which the wet surface expands. The phenomena have been described in terms of the drop height, the deadrise angle and the thickness of the shell. The studied configuration is a cone which is clamped along its outer boundary. Another case has been studied but not detailed here, which is a cone with a free outer edge. This case, which will be described in future works, gives more insight into the formation of the air pocket.

It appears that for the studied configuration, the deadrise angle mainly influences the elastic behaviour. The analysis of the penetration into the liquid shows that two different stages can be distinguished: before and after the instant when the first mode dominates.

The present model cannot be used after complete immersion is reached since the separation of the flow at the knuckle (along the outer edge of the cone) is not modelled. But the analysis of the differential system should exhibit the state of the dynamic system when the free vibration phase is supposed to start. In particular a new set of eigenfrequencies (lower than the "dry" eigenfrequencies) can be determined. This is a line of research for future work.

Experimental data for stress or deformation are not yet available. However it is strongly recommended to undertake comparisons with these quantities in order to define more precisely the domain of application for this approach.

Acknowledgements

This work is partly supported by Direction Générale pour l'Armement, and CEPM project M6406/01 in partnership with Bureau Veritas, Saipem SA (formerly Bouygues Offshore) and Principia RD.

Appendix A

Some detailed analytical calculations (when possible) are presented in these appendices.

A.1. Calculation of the vector $\mathbf{Q}(a)$

The following integrals are useful to calculate the variables $Q_m(a)$:

$$\int_0^{\pi/2} \sin\theta \mathrm{J}_0(K\sin\theta)\,\mathrm{d}\theta = \frac{\sin K}{K}, \quad \text{and} \quad \int_0^{\pi/2} \sin\theta \mathrm{I}_0(K\sin\theta)\,\mathrm{d}\theta = \frac{\sinh K}{K}, \tag{A.1}$$

$$\int_0^{\pi/2} \sin\theta \mathrm{Y}_0(K\sin\theta)\,\mathrm{d}\theta = \frac{2}{\pi K}[\mathrm{Ci}(K)\sin K - \mathrm{Si}(K)\cos K], \tag{A.2}$$

where Si and Ci are Sine and Cosine integrals (see formulæ AS 5.2.1 and AS 5.2.2). The following series can also be used:

$$\int_0^{\pi/2} \sin\theta \left[\mathrm{Y}_0(K\sin\theta) + \frac{2}{\pi}\mathrm{K}_0(K\sin\theta)\right]\mathrm{d}\theta = \frac{4}{\pi}\sum_{p=0}^{\infty} \frac{K^{4p+2}}{\Gamma(4p+4)}[\Psi(4p+4) - \log K], \tag{A.3}$$

where Γ is the Error function and Ψ denotes Γ'/Γ. This series is not very stable as soon as $K > 8$. It is hence preferable to compute the series numerically at least for the integral for K_0. For most integrals a Simpson algorithm with 100 points is used. The variable $Q_m(a)$ is plotted in Fig. 27 for the first eight modes as a function of a.

A.2. Calculation of the vector $\mathbf{g}(a)$

The coefficients $g_m(a)$ follow from Eq. (51) and they are expressed in terms of two contributions

$$g_m(a) = -\frac{2Va^3}{\pi}[Q_m(a) - Q_m^{(3)}(a)], \tag{A.4}$$

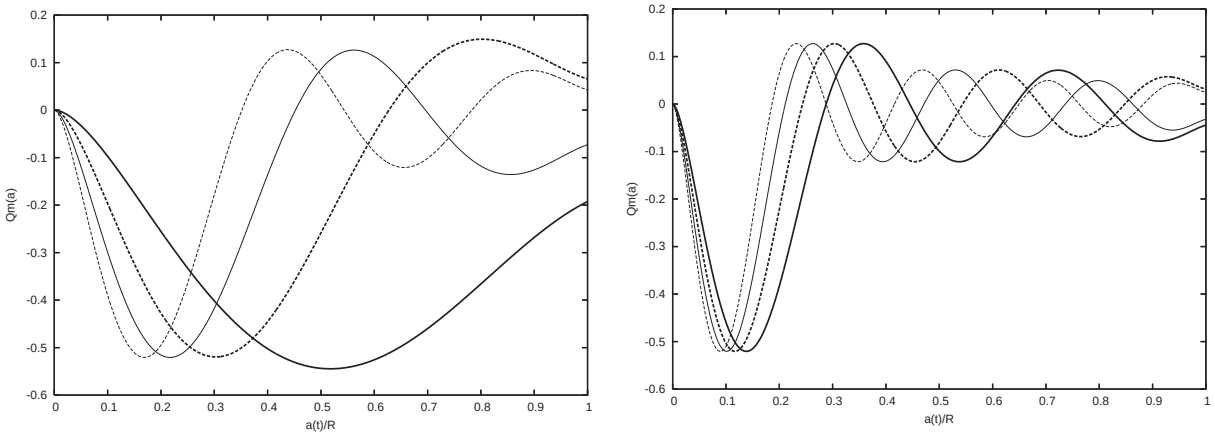

Fig. 27. Variation of $Q_m(a)$ (Eq. (24)) for the first eight modes as a function of a/R. Left: Mode No. 1: (thick solid line), No. 2: (thick dashed line), No. 3: (thin solid line), No. 4: (thin dashed line). Right: Mode No. 5: (thick solid line), No. 6: (thick dashed line), No. 7: (thin solid line), No. 8: (thin dashed line).

where $Q_m^{(3)}(a)$ is another tabulated function which is partly calculated from formulæ

$$\int_0^{\pi/2} \sin^3\theta \mathrm{J}_0(K\sin\theta)\,\mathrm{d}\theta = \frac{(K\cos K - \sin K + K^2\sin K)}{K^3}, \tag{A.5}$$

$$\int_0^{\pi/2} \sin^3\theta \mathrm{I}_0(K\sin\theta)\,\mathrm{d}\theta = \frac{(\sinh K - K\cosh K + K^2\sinh K)}{K^3}. \tag{A.6}$$

Concerning the integrals which contain Y_0 and K_0,

$$\int_0^{\pi/2} \sin^3\theta \left[\mathrm{Y}_0(K\sin\theta) + \frac{2}{\pi}\mathrm{K}_0(K\sin\theta)\right]\mathrm{d}\theta \tag{A.7}$$

a numerical integration is performed. Fig. 28 shows the variations of $g_m(a)$ for the first eight modes.

A.3. Calculation of the matrix $\mathbf{W}(a)$

The coefficients of the matrix $\mathbf{W}(a)$ are expressed in Eq. (51). Fig. 29 shows their variations with $a(t)/R$. The first four diagonal terms are compared to each other and the first four terms of the first line of the matrix as well. It is shown that the first mode is clearly dominant compared to others. This suggests that the approximation where only the first mode is used can be acceptable at least after mid-immersion. This approximation is also discussed in Ref. [37] for the two-dimensional case.

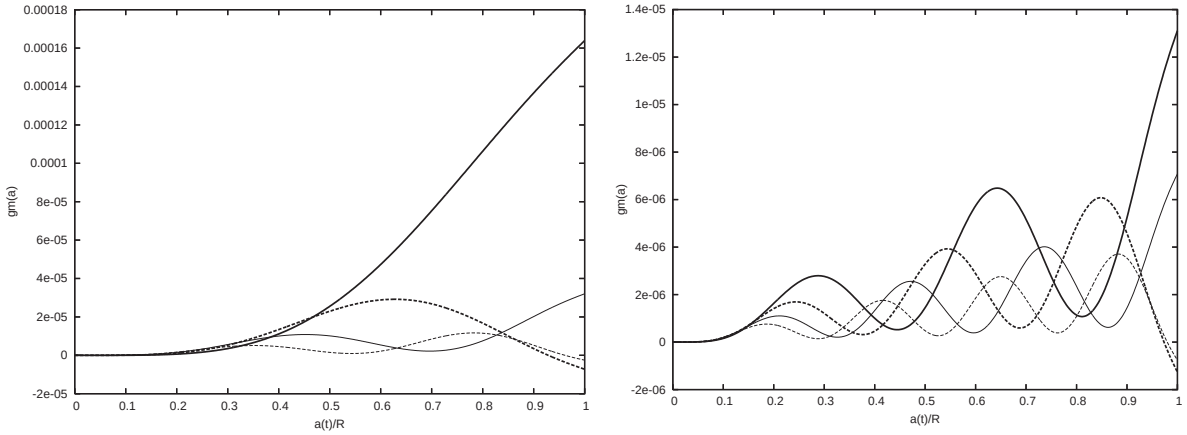

Fig. 28. Variation of $g_m(a)$ (Eq. (A.4)) for the first eight modes as a function of a/R. Left: Mode No. 1: (thick solid line), No. 2: (thick dashed line), No. 3: (thin solid line), No. 4: (thin dashed line). Right: Mode No. 5: (thick solid line), No. 6: (thick dashed line), No. 7: (thin solid line), No. 8: (thin dashed line).

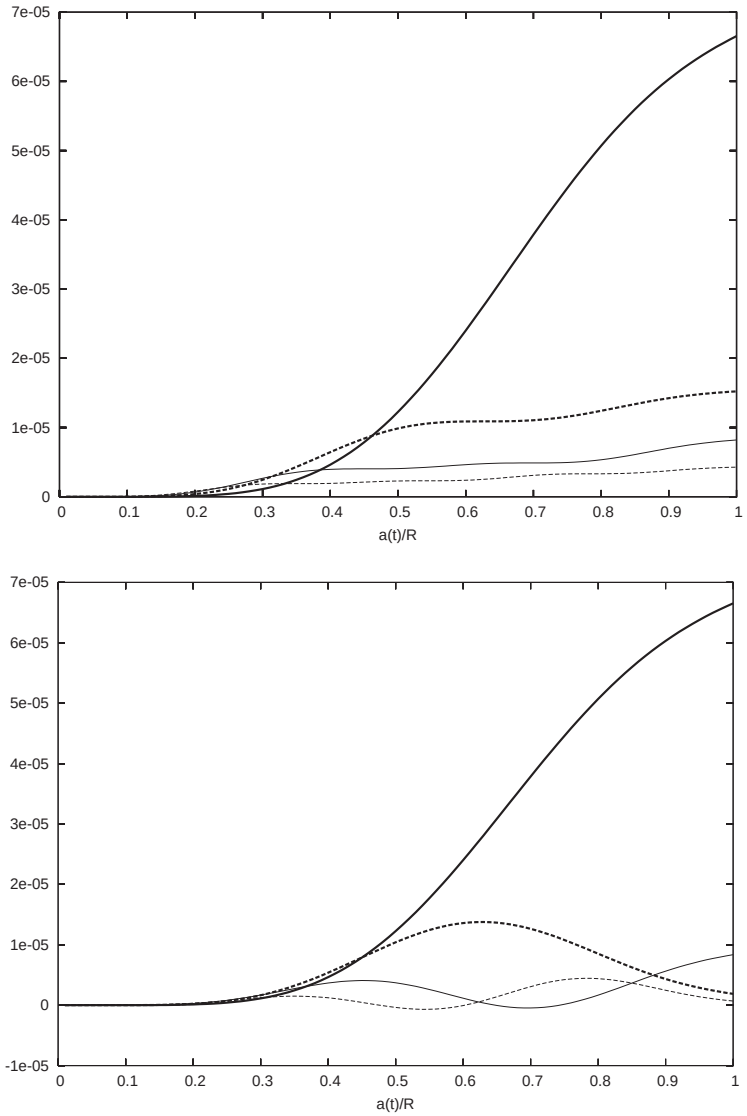

Fig. 29. Variations of the matrix coefficients $W_{mn}(a)$ as a function of a/R. Top: first four diagonal terms: $W_{nn}(a)$ with $n = 1$ (thick solid line), $n = 2$ (thick dashed line), $n = 3$ (thin solid line) and $n = 4$ (thin dashed line). Bottom: first four terms of the first line: $W_{1n}(a)$ with $n = 1$ (thick solid line), $n = 2$ (thick dashed line), $n = 3$ (thin solid line) and $n = 4$ (thin dashed line).

A.4. Modal component of the potentials

Finally, concerning the modal component of the displacement potential, in order to be calculated numerically, it is advantageously turned into

$$\Phi_m(r, a) = \frac{2r}{\pi} \int_0^{\operatorname{argch}(a/r)} \cosh x Q_m(r \cosh x)\, \mathrm{d}x. \tag{A.8}$$

Its time derivative is calculated directly from equation

$$\dot{\Phi}_n(r,a) = \frac{2a\dot{a}Q_n(a)}{\pi\sqrt{a^2-r^2}}. \tag{A.9}$$

This is useful to extract the singular part of the pressure distribution.

A.5. Modal component of the force

The variables $R_n(a)$ follow from Eq. (41). They are calculated numerically when the integrand contains the Bessel functions $(\mathrm{Y}_0, \mathrm{K}_0)$. But the following analytical formulæ are used for Bessel functions J_0 and I_0:

$$\int_0^a y\frac{\sin Ky}{K}\,\mathrm{d}y = \frac{(\sin Ka - Ka\cos Ka)}{K^3}, \tag{A.10}$$

and

$$\int_0^a y\frac{\sinh Ky}{K}\,\mathrm{d}y = \frac{(Ka\cosh Ka - \sinh Ka)}{K^3}. \tag{A.11}$$

References

[1] A. Rompteaux, J.P. Vila, Calcul du tossage avec "smart fluids", un code de calcul pariculaire compressible, *Actes des 7ieme Journées de l'Hydrodynamique*, Marseille, France, 1999, pp. 151–164.

[2] H. Wagner, Über Stoss- und Gleitvorgänge an der Oberfläche von Flüssigkeiten, *ZAMM* 12 (1932) 193–215.

[3] Y. Toyama, Two-dimensional water impact of unsymmetrical bodies, *Journal of the Society of Naval Architects of Japan* 173 (1993) 285–291 (in Japanese).

[4] R. Zhao, O.M. Faltinsen, Water entry of two-dimensional bodies, *Journal of Fluid Mechanics* 246 (1992) 593–612.

[5] R. Zhao, O.M. Faltinsen, J. Aarnes, Water entry of arbitrary two-dimensional sections with and without flow separation, *Proceedings of the ONR*, Trondheim, Norway, 1996.

[6] R. Zhao, O.M. Faltinsen, Water entry of arbitrary axisymmetric bodies with and without flow separation, *22nd Symposium on Naval Hydrodynamics*, Washington, DC, 1998.

[7] A.A. Korobkin, Initial asymptotics of solution of three-dimensional problem on a blunt body penetration into ideal liquid, *Doklady Akademii Nauk SSSR* 283 (1985) 838–842.

[8] A.A. Korobkin, V.V. Pukhnachov, Initial stage of water impact, *Annual Review of Fluid Mechanics* 20 (1988) 159–185.

[9] Y. Toyama, Flat plate approximation in the three-dimensional slamming, *Journal of the Society of Naval Architects of Japan* 179 (1996) 271–279.

[10] Y.-M. Scolan, A.A. Korobkin, Three-dimensional theory of water impact. Part 1. Inverse Wagner problem, *Journal of Fluid Mechanics* 440 (2001) 293–326.

[11] J.P.D. Wilkinson, A.P. Capelli, R.N. Salzman, Hydroelastic interaction of shells of revolution during water impact, *American Institute of Aeronautics and Astronautics Journal* 6 (5) (1968) 792–797.

[12] J. Kvålsvold, Hydroelastic Modelling of Wetdeck Slamming on Multihull Vessels, Ph.D. Thesis, University of Trondheim, Trondheim, 1994.

[13] A.A. Korobkin, T.I. Khabakhpasheva, Periodic wave impact onto an elastic plate, *Seventh Conference of Numerical Ship Hydrodynamics*, Nantes, 1999.

[14] D. Battistin, A. Iafrati, Impact of a 2D and axisymmetric bodies with arbitrary section on the water surface, *ECCOMAS CFD Conference*, Swansea, UK, 2001.

[15] B. Molin, R. Cointe, E. Fontaine, On energy arguments applied to the slamming force, *11th International Workshop on Water Waves and Floating Bodies*, Hamburg, 1996.
[16] A.A. Korobkin, Blunt-body penetration into a slightly compressible liquid, in: *Proceedings of the 20th Symposium on Naval Hydrodynamics*, Vol. 3, Santa Barbara, CA, 1994, pp. 179–186.
[17] B. Donguy, Etude de l'Interaction Fluide Structure Lors de l'Impact Hydrodynamique, Ph.D. Thesis, University of Nantes, Nantes, 2002.
[18] Z.N. Dobrovol'skaya, On some problems of similarity flow of fluid with a free surface, *Journal of Fluid Mechanics* 36 (1969) 805–829.
[19] O.F. Hughes, Solution of the wedge entry problem by numerical conformal mapping, *Journal of Fluid Mechanics* 56 (1972) 173–192.
[20] X. Mei, Y. Liu, D.K.P. Yue, On the water impact of general two-dimensional sections, *Applied Ocean Research* 21 (1999) 1–15.
[21] C.H. Lu, Y.S. He, G.X. Wu, Coupled analysis of nonlinear interaction between fluid and structure during impact, *Journal of Fluid Structures* 14 (2000) 126–146.
[22] K. Marguerre, Zur Theorie der gekrümmten platte grosser Formänderung, Jahrbuch des 1939 der Deutschen Luftfahrforschnung, 1933, p. 413.
[23] S. Soliman, P.B. Gonçalves, Chaotic behavior resulting in transient and steady state instabilities of pressure-loaded shallow spherical shells, *Journal of Sound and Vibration* 259(3) 497–512.
[24] F.Y.M. Wan, On the equations of the linear theory of elastic conical shells, *Stud. Appl. Math* XLIX (1) (1970) 69–83.
[25] R.V. Southwell, On the free transverse vibrations of a uniform circular disk clamped at its center; and on the effects of rotation, *Proceedings of the Royal Society, London* 101 (1922) 133–153.
[26] S.M. Vogel, D.W. Skinner, Natural frequencies of transversely vibrating uniform annular plates, *Journal of Applied Mechanics, Transactions of the American Society of Mechanical Engineers* 32 (1965) 926–931.
[27] A.A. Korobkin, Y.-M. Scolan, Asymptotic analysis of three-dimensional water impact, *17th International Workshop on Water Waves and Floating Bodies*, Cambridge, UK, 2002.
[28] M.K. Kwak, Vibration of circular plates in contact with water, *Transactions of the American Society of Mechanical Engineers* 58 (1991) 480–483.
[29] I.N. Sneddon, *Mixed Boundary Value Problems in Potential Theory*, Wiley, New York, 1966.
[30] M. Abramowitz, I.A. Stegun, *Handbook of Mathematical Functions*, Dover, New York, 1979.
[31] I.S. Gradshteyn, I.M. Ryzhik, *Tables of Integrals*, 5th Edition, Academic Press, New York, 1994.
[32] Y.-M. Scolan, A.A. Korobkin, The energy distribution from impact of a three-dimensional body onto a liquid free surface, *16th International Workshop on Water Waves and Floating Bodies*, Hiroshima, 2001.
[33] Y.-M. Scolan, A.A. Korobkin, Energy distribution from vertical impact of a three-dimensional solid body onto the flat free surface of an ideal fluid, *Journal of Fluids and Structures* 17 (2003) 275–286.
[34] J.N. Newman, *Marine Hydrodynamics*, MIT Press, Cambridge, MA, 1977.
[35] Y.-M. Scolan, A.A. Korobkin, On energy arguments applied to slamming of elastic body, in *Proceedings of the Third International Conference on Hydroelasticity in Marine Technology*, Oxford, UK, September 2003.
[36] O.M. Faltinsen, Hydroelastic slamming, *Journal of Marine Science and Technology* 5 (2) (2000) 49–65.
[37] T.I. Khabakhpasheva, A.A. Korobkin, Approximate models of elastic wedge impact, *18th International Workshop on Water Waves and Floating Bodies*, Le Croisic, France, 2003.
[38] H. Bredmose, D.H. Peregrine, A. Porter, G.N. Bullock, Wave impact and aerated water, *18th International Workshop on Water Waves and Floating Bodies*, Le Croisic, France, 2003.